Journal of Asian Earth Sciences: X 9 (2023) 100136

Contents lists available at ScienceDirect

Journal of Asian Earth Sciences: X

journal homepage: www.sciencedirect.com/journal/journal-of-asian-earth-sciences-x

Elemental abundances and isotopic composition of Italian limestones: Glimpses into the evolution of the Tethys

Gianluigi Rosatelli [a,*], Francesca Castorina [b,c], Ada Consalvo [a], Francesco Brozzetti [a], Domenico Ciavardelli [a,d], Maria Grazia Perna [a], Keith Bell [e], Simone Bello [a], Francesco Stoppa [a]

[a] Università "G. d'Annunzio", Via dei Vestini 31, 66100 Chieti, Italy
[b] Università "La Sapienza" - Piazzale Aldo Moro 5, 00185 Roma, Italy
[c] Consiglio Nazionale delle Ricerche, IGAG, c/o Dipartimento di Scienze della Terra, Università di Roma "La Sapienza", Italy
[d] Università degli Studi di Enna "Kore", Cittadella Universitaria, 94100 Enna, Italy
[e] Ottawa-Carleton Geoscience Centre, Dept. of Earth Sciences, Carleton University, 1125 Colonel By Drive, Ottawa, ON K1S 5B6, Canada

ARTICLE INFO

Keywords:
Limestone
Isotopes
Major and trace elements
Tethys
Italy

ABSTRACT

Biogenic limestones from three sections (north, central, and south) across peninsular Italy have been analysed for major and trace elements and Nd, Pb, and Sr isotopic ratios. These data are used to monitor the evolution of the Tethys Ocean from the Triassic through to the Miocene. Limestones' major, trace, and REE elements contents are consistent with their formation in seawater with little sign of crustal, volcanic, or hydrothermal input. V/Cr and Ce/Ce* ratios indicate their deposition in oxygenated waters. Rb-Sr-Ba discrimination diagram, consistent with the immobile trace element distribution, indicates that limestone deposition took place in either marginal or open ocean environments. Ages based on stratigraphy are in good agreement with the chronostratigraphic Sr curves implying that the Tethys ocean, throughout its history, was in contact with the open, global, ocean system. Although the isotopic values of Sr and Nd are relatively restricted, Pb is extremely variable and highly radiogenic. High Pb isotope ratios characterise limestones deposited during the rifting of the southern Tethyan ocean in the Lower Jurassic and in the Lower Cretaceous, suggesting stronger crustal inputs in small basins. The weighted average, present-day, isotope values (AIL = average Italian limestone) for the Italian limestones, excluding anomalous samples, are $^{87}Sr/^{86}Sr = 0.70785$, $^{143}Nd/^{144}Nd = 0.51227$, and $^{206}Pb/^{204}Pb = 18.94$, $^{207}Pb/^{204}Pb = 15.69$, $^{208}Pb/^{204}Pb = 38.66$. These values are useful in monitoring the fate of limestones during orogenesis and the role that they may have played in magma genesis.

1. Introduction

Most of the upper crust of peninsular Italy, including the Apennines, is made up of a thick succession of limestones reflecting carbonate deposition during the evolution of the NeoTethys ocean. Although there have been many isotopic studies of limestones from the Mediterranean region, especially C and O (e.g. Jenkyns and Clayton, 1986; Huck et al., 2013; Gambacorta et al., 2015) as well as Sr and Nd (e.g. Dera et al. 2015; Cornacchia et al., 2018 and references therein), few have included analyses of Sr, Nd, Pb, from the same samples along with their major, and trace elements. The intent of this paper is to provide a Sr, Nd, and Pb isotopic database for the limestones, as well as whole-rock and trace-element data that can be used to monitor the composition of seawater, thus insights into the contributions of terrigenous intake, hydrothermal inputs, diagenetic modifications, and overall tectonic settings (eg. Zhang et al., 2017; Frank, 2002).

During Late Paleozoic – Early Mesozoic times, the central Mediterranean area hosted several carbonate platforms separated by euxinic basins (e.g. Zarcone et al., 2010; Cosentino et al., 2010). In Italy, as a consequence of the NeoTethys Jurassic rifting, and the following Cretaceous to present convergence, the paleogeography of the different domains continuously evolved along with concurrent sedimentation, leading to several, greatly diversified, stratigraphic successions (Figs. 1 and 2).

The geometric relationships that existed between these successions in pre-orogenic times are not easy to reconstruct, due to the large tectonic transport that occurred during the Neogene along both east-verging overthrusts and regional-scale wrench faults (Cosentino et al.,

* Corresponding author.
E-mail address: g.rosatelli@unich.it (G. Rosatelli).

https://doi.org/10.1016/j.jaesx.2023.100136
Received 30 August 2022; Received in revised form 29 December 2022; Accepted 3 January 2023
Available online 7 January 2023

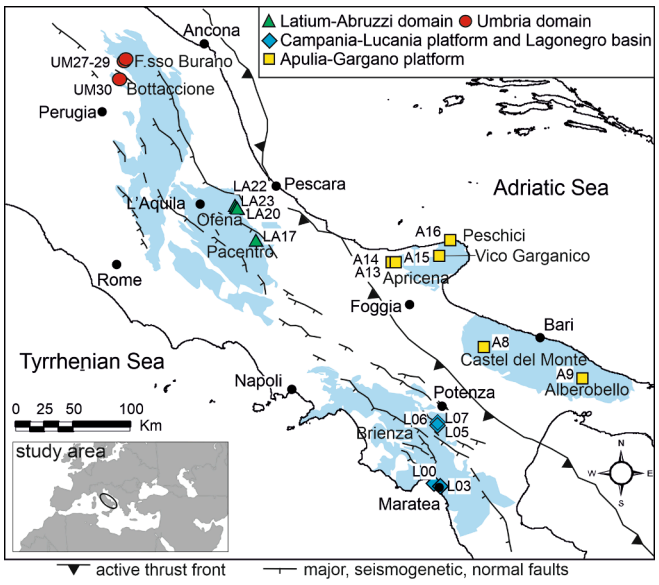

Fig. 1. Map showing the Tethyan sedimentation domains in Central-Southern Apennines and sampling localities. Sampling sites: Maratea and Brienza for Lagonegro platform/basin; Alberobello, Castel del Monte, Apricena, Vico Garganico, Peschici, for Apulian Garganic platform; Pacentro and Ofena for Lazio-Abruzzi sequence and F.sso Burano and Bottaccione for Umbria-Marche sequence. In light blu are reported the main areas where Triassic-Miocene limestones outcrop. The major active faults reported are from Brozzetti et al. (2017); Lavecchia et al. (2021); Lavecchia et al. (2022); Bello et al. (2022). The inset shows the study area.

2010).

According to a widely accepted model (Patacca et al., 2008 and reference therein), in the central-southern Apennines, a major carbonate shelf, referred to as the Apennine Platform, bordered the east side of the Tethyan ocean. Most of the shallow water carbonates outcropping in the chain, ascribed to the Latium-Abruzzi and Campania-Lucania platforms (Fig. 2a), belong to this internal domain.

Two main pelagic basins developed southeast and north of the Apennine Platform. The first one, known as the Lagonegro-Molise basin (stratigraphy in Fig. 2b and 2c), was set up earlier, straddling the Middle-Late Triassic boundary and recording pelagic conditions until the early Miocene; according to Zarcone et al. (2010), it had discontinuous connections with the Ligurian branch of Neo Tethys.

The second one, or Umbria-Marche basin, originated during the Early Jurassic extensions which caused intense subsidence and the drowning of a paleo-platform that previously extended over the entire central-northern Apennines (Calcare Massiccio epeiric platform). The stratigraphy of the Umbria-Marche domain (Fig. 2d), reflects such a tectonic-sedimentary history, showing a vertical evolution from shallow water (Early Jurassic) to pelagic limestones (Middle Jurassic-Middle Miocene basinal multilayer).

The Lagonegro and Umbria-Marche basins were probably connected through narrow NS-oriented furrows, as suggested by the location of the marginal facies of the Abruzzi platform and the adjoining slope to basin deposits described in the column of Fig. 2b (Gran Sasso area).

The Apulian platform, outcropping northward in the Morrone-Maiella area and to the south in the Murge-Salento peninsula (stratigraphy in Fig. 2e-2f), developed at least since the Late Triassic. Here shallow water limestones sedimented up to the Late Miocene (Fig. 2f), with temporary interruptions during some significant hiatuses marked by thick paleosols or bauxite deposits.

This latter platform which, according to the palinspastic restoration was likely the greater of the central Mediterranean area (Patacca et al., 2008), was bounded eastward by the Adriatic basin, in northern communication with the Umbria-Marche domain. The east margin of the Apulia platform and the transitional facies to the Adriatic basin widely crop out in the eastern Gargano area (Fig. 2f).

Starting from the Langhian-Serravallian, the contractional tectonics involved the western part of the Adria plate, giving rise to major thrusts whose strikes were not always parallel to the edges of the aforementioned paleogeographic domains. Consequently, the accretion of these latter into the chain was not isochronous from north to south. The paper focuses on the geochemical characterization of limestones to assess the relations between the local basins and the Tethyan ocean. In addition, we tested the geochemical signal recorded in the limestones of major geodynamic events occurring during the development of the European-Africa margins from the Triassic to the Miocene.

2. Materials and methods

The sample suite studied, although timely discontinuous, gives an overview of the evolution of the carbonate succession along the European and African margins and their relationship with the geodynamic changes that influenced lithosphere metasomatism, magmatism, continental weathering-orogenesis, and global oceanic circulation.

Fig. 1 displays the distribution of limestones in peninsular Italy and our sampling localities. Samples were collected along three, roughly east–west sections representing respectively a southern, central and northern section. Limestones of the southern section were collected from Maratea and Brienza (sample code L = Lagonegro sequence), Peschici, Vico Garganico, Apricena, Castel del Monte, and Alberobello (sample code A = Apulia platform). Sampling localities of the central section were Pacentro and Ofena near L'Aquila (sample code LA = Abruzzo-Lazio sequence), while F.sso Burano and Bottaccione (sample code UM = Umbria-Marche sequence) were sampled for the northern section (Fig. 1). Table 1 displays details of the sampling sites, Dunham's classification, and depositional paleo-environment of the limestones. Limestones are mudstone, packstone, and wackestone and represent a large part of the last 200 Ma evolution of the NeoTethys Ocean, the oldest Triassic age and the youngest of the Upper Miocene.

Samples were carefully selected in the field to be sure they were homogeneous and fresh. In the laboratory, aliquots needed for each analytical procedure were selected after crushing the hand specimen with the hammer and the pieces were checked under an optical magnifier to avoid the presence of spaty carbonate patches, dissolution/recrystallization features like stylolites, or secondary veins.

The selected samples were then crushed in an agate mill. Bulk rock major elements were determined at SARM (CNRS Nancy, France) by IPC-AES following the method of Carignan et al. (2001).

At Carleton University, samples were crushed in an agate mortar to <100 mesh and 10 mg powder was dissolved using 2.5 N HCl. For further details of the analytical procedures, see Mirnejad and Bell (2006). Isotopic analyses of Sr, Nd, and Pb were made using a Finnigan-MAT 261 multi-collector, solid-source mass spectrometer operated in the static mode.

All of the Pb isotopic ratio measurements were performed at Carleton University. For analytical details, see Owen (2006). Standards run during the course of this study at Carleton yielded the following values: NBS-987 $^{87}Sr/^{86}Sr$ = 0.71025 ± 0.00003, La Jolla $^{143}Nd/^{144}Nd$ = 0.51187 ± 0.00003, NBS-981 $^{206}Pb/^{204}Pb$ = 16.890 ± 0.010, $^{207}Pb/^{204}Pb$ = 15.429 ± 0.013, $^{208}Pb/^{204}Pb$ = 36.498 ± 0.042. Uncertainties are given at the 2σ level. The measured Sr and Nd isotopic ratios for all samples were corrected for fractionation to $^{88}Sr/^{86}Sr$ = 8.3752 and $^{146}Nd/^{144}Nd$ = 0.7219. An average fractionation factor of 0.12 per mass unit was applied to all measured Pb isotope ratios based on repeated analyses of NBS-98. Procedural blanks are Nd: 60 pg, Pb: 80 pg, and Sr: 150 pg.

At the University of Rome, La Sapienza, samples were crushed in an agate mortar to < 100 mesh, and approximately 500 mg of powders were dissolved with 10 mL of 2.5 M ultrapure HCl. 10 % aliquots of each solution were used to separate Sr from the matrix for isotopic analysis

and the remainder was used for REE concentration (Sharma and Wasserburg, 1996). To change the pH of the solution to 9.0 for precipitating REE-rich Fe–Al oxi-hydroxides, NH_3 was added. Both the precipitate and supernatant were mixed with a vortex overnight and separated by centrifugation. Oxi-hydroxides were dissolved with 4 M HCl and the solution evaporated. Sr and REE were separated from the matrix onto Bio-Rad AG50W-X12 resin, following the procedure of Chao-Feng et al. (2014), whereas the separation of Nd from other REE was carried out in 2-ml columns filled with Ln. Spec resin (Triskem-international) following Pin and Zalduegui (1997). Isotopic analyses were carried out at IGAG-CNR, Dipartimento di Scienze della Terra, University of Rome "La Sapienza" using a FINNIGAN MAT 262RPQ multi-collector, mass spectrometer using W single and Re double filaments in the static mode for Sr and Nd, respectively. Sr and Nd isotopic fractionations were corrected using $^{86}Sr/^{88}Sr = 0.1194$ and $^{146}Nd/^{144}Nd = 0.7219$, respectively. During the data acquisition, measured isotopic ratios of NBS 987 Sr and La Jolla Nd standards resulted as $^{87}Sr/^{86}Sr = 0.710254 \pm 10$ (2σ; n = 27) and $^{143}Nd/^{144}Nd = 0.511880 \pm 11$ (2σ; n = 10), respectively.

Measured Nd isotopic ratios were expressed as ε_{Nd}, i.e. the isotopic ratio of the sample relative to CHUR (DePaolo and Wasserburg, 1976). Total procedural blanks were below 2 and 1 ng of Sr and Nd, respectively. In spite of the different procedures and different mass spectrometers, both Nd and Sr values show no bias in measurements between the two laboratories.

The ICP-MS analysis were made at the University of Chieti, in the Analytical Biochemistry Lab. (Ce.S.I-Me.T.). The limestones were crushed in an agate mortar and ~ 10 mg powder of each sample was dissolved in 37 % HCl, freeze dried, accurately weighed and then taken into solution with 1 mL of 69 % HNO_3 then diluted to a final volume of 100 mL with 18MΩ cm water, and analysed by Inductively Coupled Plasma Mass Spectrometry (ICP-MS). ICP-MS analyses were made using a 7500A ICP mass spectrometer (Agilent Technologies, Tokyo, Japan) fitted with an ASX-510 autosampler (Cetac Technologies, Omaha, NE) and a peristaltic pump. A Babington nebulizer with a Scott spray chamber (Agilent Technologies) was used for sample introduction. The following operating conditions were applied: forward power = 1260 W; plasma gas flow rate = 15L min-1; carrier gas flow rate = 1.13L min-1; spray chamber temperature = 2 °C; sampler and skimmer cone: Ni, 1 and 0.4 mm inside diameter, respectively; sample uptake rate = 0.4 mL min-1; sample depth = 7 mm; sampling period per mass = 0.3 s (three replicates) (Ciavardelli et al., 2007; Ciavardelli et al., 2010). The operating conditions were optimized for the best sensitivity using a 10 mg/L solution of ^{7}Li, ^{89}Y and ^{205}Tl and for the reduction of $^{140}CeO^{+}/^{140}Ce^{+}$ and $^{140}Ce^{2+}/^{140}Ce^{+}$ ratios below 1 % and 3 %, respectively. The sample introduction system was washed between different analyses with 2 %

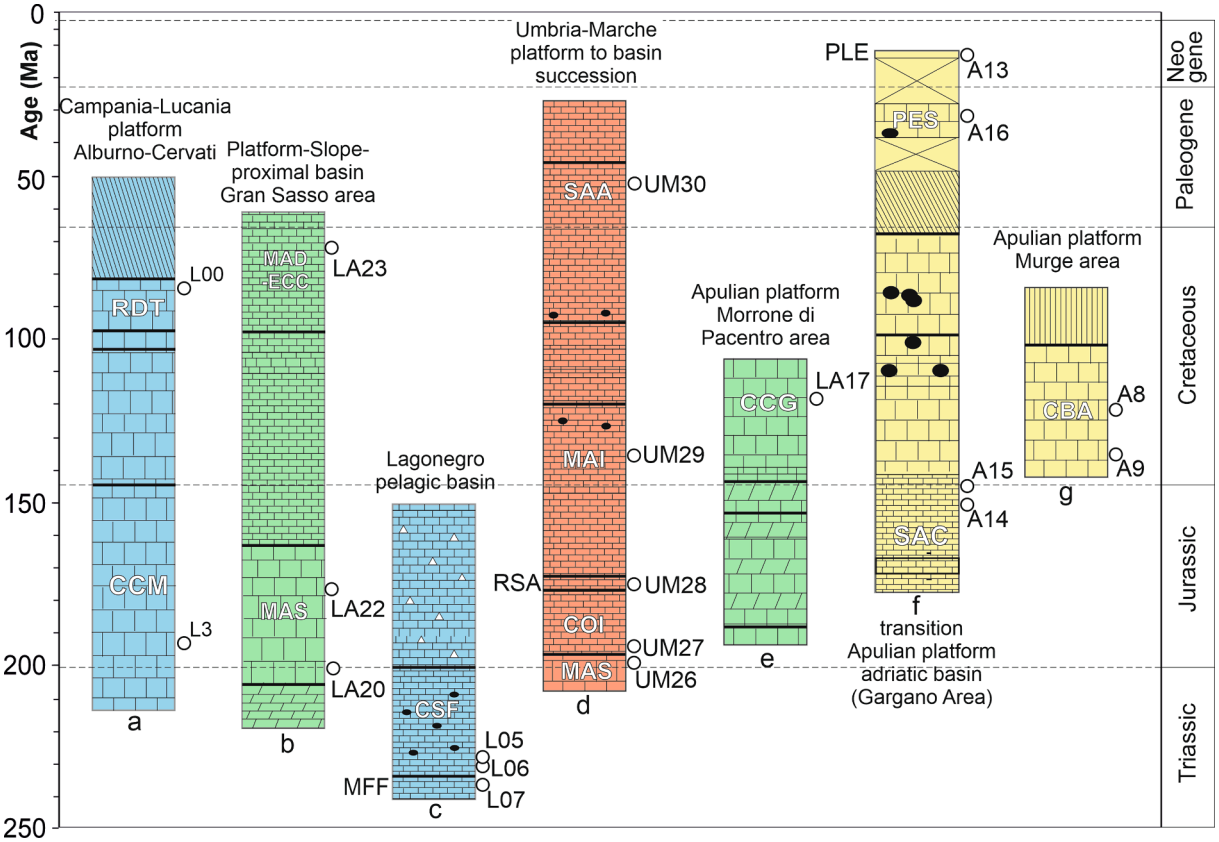

Fig. 2. Stratigraphic schemes are representative of the different paleogeographic domains recognized in the central-southern Apennines (details in the text). The length of the columns is related to the time-extent of each succession (reported in Ma on the vertical axis) and not to their actual thickness (i.e. not to scale). The labeled empty circles show the position of the analyzed samples on the related geological formation whose acronym is reported on the column; such acronyms correspond to the abbreviations used in the official cartography on a scale of 1:50,000, published by the National Geological Survey of Italy (CARG project, available at https://www.isprambiente.gov.it/Media/carg/) Key to lithological hatches: large bricks = shallow-water platform limestones; bricks with oblique bars = shallow water dolostones; small bricks = pelagic limestones; small bricks with triangles = radiolarites alternating with siliceous limestones; small bricks with full black circles = cherty limestones.Formation acronyms (from left to right column): *Column a*) CCM = Cladocoropsis and Clypeina Limestones; RDT = Radiolitid bearing limestones (CARG Project, Sapri); *Column b*) MAS= "Calcare Massiccio" fm; ECC = crystalline limestones with echinoderms and corals; MAD = detrital "Maiolica" (CARG Project, "Torre de Passeri"); *Column c*) MFF= "Monte Facito" fm; CSF= "Calcari con Selce" fm (Vitale et al., 2020); *Column d*): MAS="Calcare Massiccio" fm; COI= "Corniola", RSA = "Rosso Ammonitico"; MAI = "Maiolica", fm; SAA= "Scaglia Rossa" fm (CARG Project, "Cagli"); *Column e*): CCG = gastropod-bearing cyclothymic limestones (CARG Project, "Sulmona"); *Column f*): "Mt. Sacro" limestones; PES= "Peschici" fm; PLE= "Pietra Leccese" fm. (Morsilli, 2016); *Column g*): CBA = Bari limestones (Morsilli, 2016).

Table 1
Sampling location, stratigraphic and Sr dating, limestone lithology (Duhnam classification) and depositional paleo-environment (with data source).

Sample	Lat	Long	Locality	Chronostratigraphic age	Sr dating (Ma)	Lithology	Depositional environment	Formation Acronim	References
L00	40.04034	15.66184	Acquafredda di Maratea	Upper Cretaceous, Santonian	84.8	grey wackestone (rudists)	tidal flat	RDT	Compagnoni and Damiani (1971)
L03	40.014	15.727	Maratea, Potenza	Lower Jurassic, Sinemurian	193.6	grey packstone	tidal flat	CCM	Compagnoni and Damiani (1971)
L05	40.49352	15.7412	Brienza Potenza	Upper Triassic, Carnian	228.5	grey mudstone	pelagic	CSF	Scandone (1971)
L06	40.49352	15.7412	Brienza, Potenza	Upper Triassic, Carnian	231.3	grey mudstone	pelagic	CSF	Scandone (1971)
L07	40.50375	15.74945	Brienza, Potenza	Upper Triassic, Carnian	237	beige mudstone	pelagic	MFF	Scandone (1971)
A08	41.08407	16.27427	Castel del Monte, Bari	Lower Cretaceous, Valanginian	135.7	mudstone	inner platform	CBA	Spalluto et al. (2005)
A09	40.76682	17.26186	Alberobello, Bari	Lower Cretaceous, Aptian	122	packstone	tidal flats	CBA	Spalluto et al. (2005)
A13	41.80786	15.37998	Apricena, Puglia	Neogene, Miocene, Serravallian	13.3	white packstone	open platform	PLE	Moretti et al. (2011)
A14	41.80661	15.42092	Apricena, Puglia	Upper Jurassic, Tithonian	151.1	mudstone	open lagoon	SAC	Moretti et al. (2011)
A15	41.8331	15.88456	Vico, Gargano, Puglia	Upper Jurassic, Tithonian	145.4	white packstone	platform margin	SAC	Morsili et al. (2017)
A16	41.949	16.011	Peschici, Foggia	Paleogene Oligocene, Rupelian	31.87	mudstone	shallow basin	PES	Morsili et al. (2017)
LA17	42.05	13.966	Pacentro, L'Aquila	Lower Cretaceous, Aptian	118.64	light grey mudstone	platform	CCG	Centamore et al. (2006a)
LA20	42.33234	13.76125	Ofena, L'Aquila	Upper Triassic, Hettangian	201.3	mudstone breccia	platform	MAS	Centamore et al. (2006b)
LA22	42.31915	13.77209	Ofena, L'Aquila	Lower Jurassic, Toarcian	177	white mudstone	platform margin	MAS	Centamore et al. (2006b)
LA23	42.31196	13.78877	Ofena, L'Aquila	Upper Cretaceous, Campanian	72.3	white mudstone	platform	MAD-EDC	Centamore et al. (2006b)
UM26	43.50966	12.63969	Burano Valley Cagli	Lower Jurassic, Hettangian/Sinemurian	199.6	massive mudstone	tidal flat	MAS	Barchi et al. (1993)
UM27	43.50966	12.63969	Burano Valley Cagli	Lower Jurassic, Sinemuriano	194.5	massive mudstone	pelagic	COI	Barchi et al. (1993)
UM28	43.50966	12.63969	Burano Valley Cagli	Middle Jurassic, Toarciano	174	reddish mudstone	pelagic	RSA	Barchi et al. (1993)
UM29	43.50966	12.63969	Burano Valley Cagli	Lower Cretaceous, Valangianian	134	white mudstone	pelagic	MAI	Barchi et al. (1993)
UM30	43.36566	12.58252	Bottaccione, Gubbio	Paleogene, Eocene, Ypresian	53	pinkish mudstone	pelagic	SAA	Galeotti et al. (2013)

HNO_3. The standard addition method was used for the quantification of Hf, Nb, Ta, and Zr, and the external standard method was used for the quantification of all other elements. An internal standard correction was performed by online addition of an internal standard solution of Rh (50 mg/L) in a *T*-piece. Data analysis was performed using ChemStation software (Agilent Technologies).

Table 2
Major elements analyses (wt%).

	Sample	SiO_2	Al_2O_3	Fe_2O_3	MnO	MgO	CaO	Na_2O	K_2O	TiO_2	P_2O_5	LOI	Total
Southern area	L00	0.08	0.04	0.04	0.001	0.34	54.58	0.015	bdl	bdl	bdl	43.85	98.94
	L03	0.09	0.08	0.04	0.0004	1.19	53.48	0.022	0.01	bdl	bdl	44.13	99.03
	L05	1.24	0.27	0.15	0.026	0.45	53.66	0.014	0.084	bdl	bdl	43.35	99.23
	L06	1.13	0.33	0.13	0.02	0.73	53.26	0.051	0.053	bdl	bdl	43.42	99.12
	L07	0.74	0.42	0.16	0.129	0.59	53.89	0.02	0.077	0.03	bdl	43.32	99.37
	A08	0.2	0.08	0.04	0.001	0.32	55.03	0.014	0.008	bdl	bdl	43.94	99.62
	A09	0.24	0.06	0.03	0.0003	0.24	54.71	0.01	bdl	bdl	bdl	43.98	99.27
	A13	1.52	0.5	0.3	0.006	0.54	52.94	0.087	0.09	0.03	0.46	42.73	99.19
	A14	0.15	0.04	0.03	0.0008	0.55	54.86	0.014	bdl	bdl	bdl	43.98	99.62
	A15	0.19	0.05	0.03	0.004	0.12	55.44	0.009	bdl	bdl	bdl	43.7	99.54
	A16	0.11	0.07	0.04	0.002	0.13	55.51	0.009	bdl	bdl	0.05	43.39	99.3
Central area	LA17	0.06	0.06	0.03	0.0008	1.32	54.28	0.017	0.008	bdl	bdl	44.11	99.89
	LA20	0.15	0.05	0.03	0.002	14.61	38.37	0.022	bdl	bdl	bdl	45.33	98.56
	LA22	0.48	0.21	0.07	0.002	1.34	53.29	0.021	0.059	bdl	bdl	43.88	99.35
	LA23	0.18	0.07	0.03	0.002	0.38	54.87	0.02	0.01	bdl	0.22	43.62	99.4
Northern area	UM26	0.16	0.07	0.03	0.003	0.51	55.11	0.011	0.018	bdl	bdl	43.57	99.49
	UM27	1.42	0.29	0.21	0.021	0.53	53.71	0.02	0.114	0.02	bdl	43.26	99.6
	UM28	3.08	0.78	0.31	0.023	0.69	52.21	0.034	0.347	0.04	bdl	42.22	99.73
	UM29	0.67	0.14	0.1	0.029	0.39	54.11	0.016	0.037	bdl	bdl	43.7	99.2
	UM30	3.87	1.13	0.45	0.129	0.35	51.77	0.038	0.216	0.06	0.06	41.54	99.6
	2σ	0.01	0.01	0.015	0.0005	0.01	0.01	0.005	0.0002	0.01	0.02		

3. Results

3.1. Major elements

Whole-rock analyses were made of 11 samples from the southern section of which 5 were from the Lagonegro basin (L) and 6 from the Apulian platform (A); 4 samples from the central section (LA) and 5 samples from the northern section (UM) (Table 2, Fig. 1). The CaO content is fairly constant with an average value of 54.04 wt% (range 51.77 to 55.51 wt%). One exception is sample LA20, which is dolomitic in composition. (CaO = 38.37 wt%, MgO = 14.61 wt%). Terrigenous-derived elements such as Si, Al, and Fe are generally low. SiO_2 ranges from 0.06 wt% to 3.87 wt%, with an average value of 0.79 wt%, Al_2O_3 varies from 0.04 wt% to 1.13 wt% with average of 0.24 wt% while Fe_2O_3 ranges from 0.03 and 0.45 wt% with an average value of 0.11 wt%.

In the limestones the correlation between CaO and SiO_2 is generally high: the linear correlation coefficient for UM samples is $R^2 = 0.98$, for LA samples $R^2 = 0.63$, A samples have $R^2 = 0.91$, while for L samples the correlation is low being $R^2 = 0.29$ (Fig. 3a). Similar relations were observed between CaO and Al_2O_3 (Fig. 3b), CaO and Fe_2O_3 (Fig. 3c), with the L samples showing the weakest linear correlation coefficient. Between CaO and MnO there is only a moderate correlation in the UM samples (Fig. 3d, R2 = 0.53) while the relations are very poor for all the rest of the sample set.

3.2. Trace elements

Large ion lithophile elements (LILE), high field strength elements (HFSE) and transition metals have been normalized to upper continental crust (UCC, McLennan, 2001) and shown in Fig. 5. The limestones, as expected, have much lower trace elements contents than average upper crust (i.e. < 1), except for Sr and U. The latter show a strong, positive peak, with the exception of samples UM28 and UM30 where $Pb_{UCC} > U_{UCC}$ (Fig. 5d). Th_{UCC} is generally lower than U_{UCC} showing a negative anomaly but in samples UM28 and UM30 (Fig. 5d). Rb is invariably depleted with respect to the other LILE (Fig. 5a-d). Ba presents a positive spike ($Ba_{UCC} > Th_{UCC}$ and $Ba_{UCC} > Rb_{UCC}$) in most of the samples of the central and southern sections but L05, L06, A13, and LA22 (Fig. 5a to 5c). However, in the northern section, only UM30 shows a strong positive Ba spike (Fig. 5d). Deep negative anomalies of HFSE (Nb, Ta, Zr, Hf) are common to all the samples and reflect the resistance to weathering of minerals rich in these elements (Taylor and McLennan, 1985) and their low solubility in water. Sr shows a strong positive anomaly in all samples (Fig. 5a to 5d). The Sr values in the limestones lie between 42 ppm and 838 ppm, with an average of 293 ppm which is lower than the average Sr content (350 ppm) of the Post-Archean Australian Shales (PAAS, Pourmand et al., 2012), commonly used as the reference reservoir for normalizing limestone values.

Overall, V, Cr, Ni, Co, and Cu, are, at least, one order of magnitude depleted in comparison to UCC values. Zn consistently shows a positive

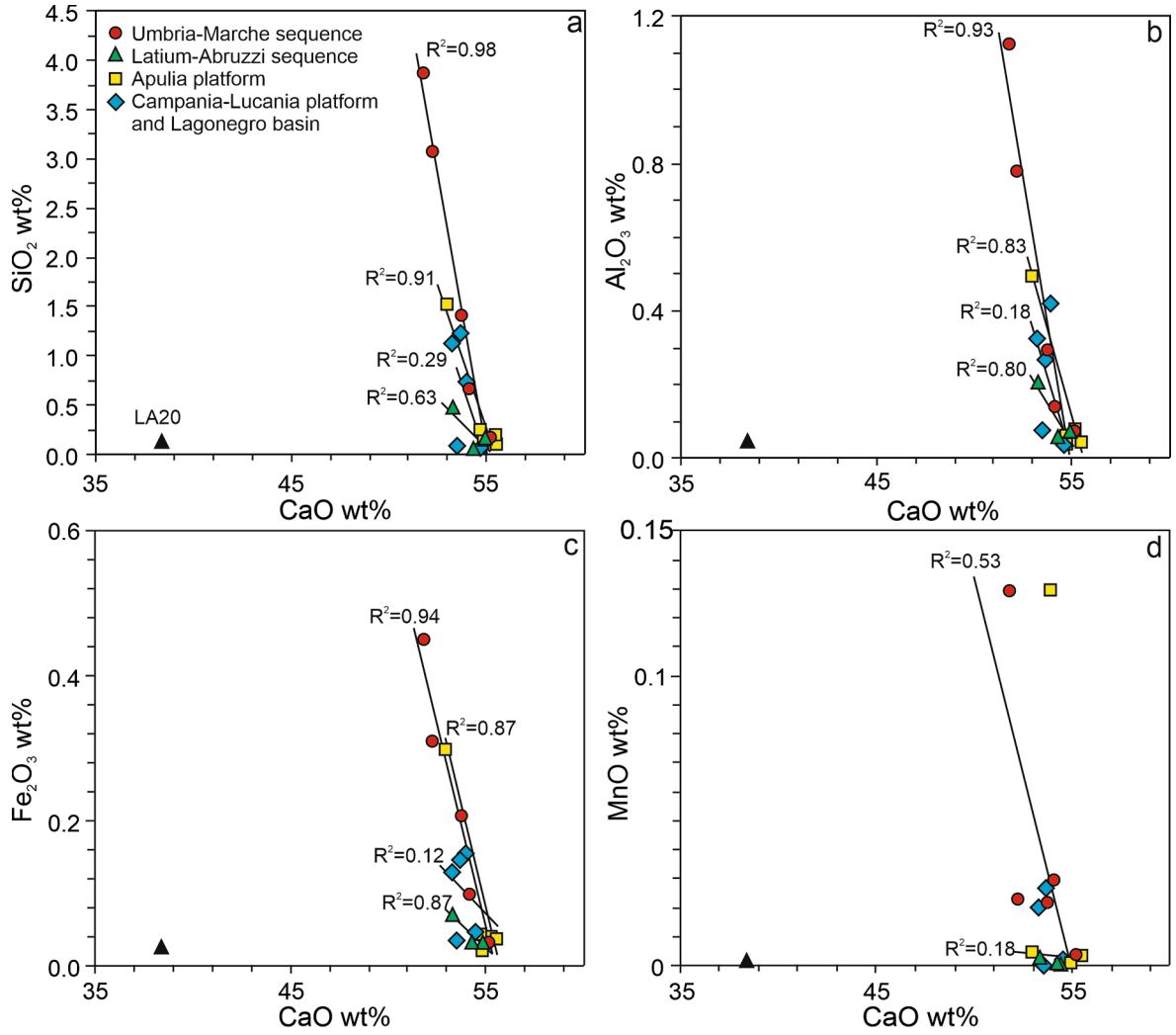

Fig. 3. Major elements variations: a) CaO vs SiO_2; b) CaO vs Al_2O_3; c) CaO vs Fe_2O_3; d) CaO vs MnO. All the elements show an inverse correlation with CaO.

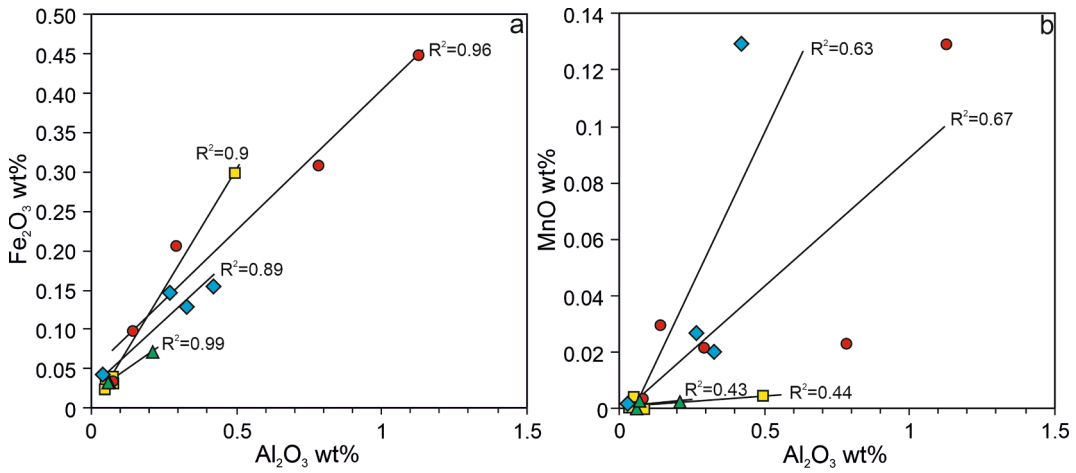

Fig. 4. Major elements variations. a) Fe_2O_3 vs Al_2O_3 and b) MnO vs Al_2O_3. Legend as Fig. 3.

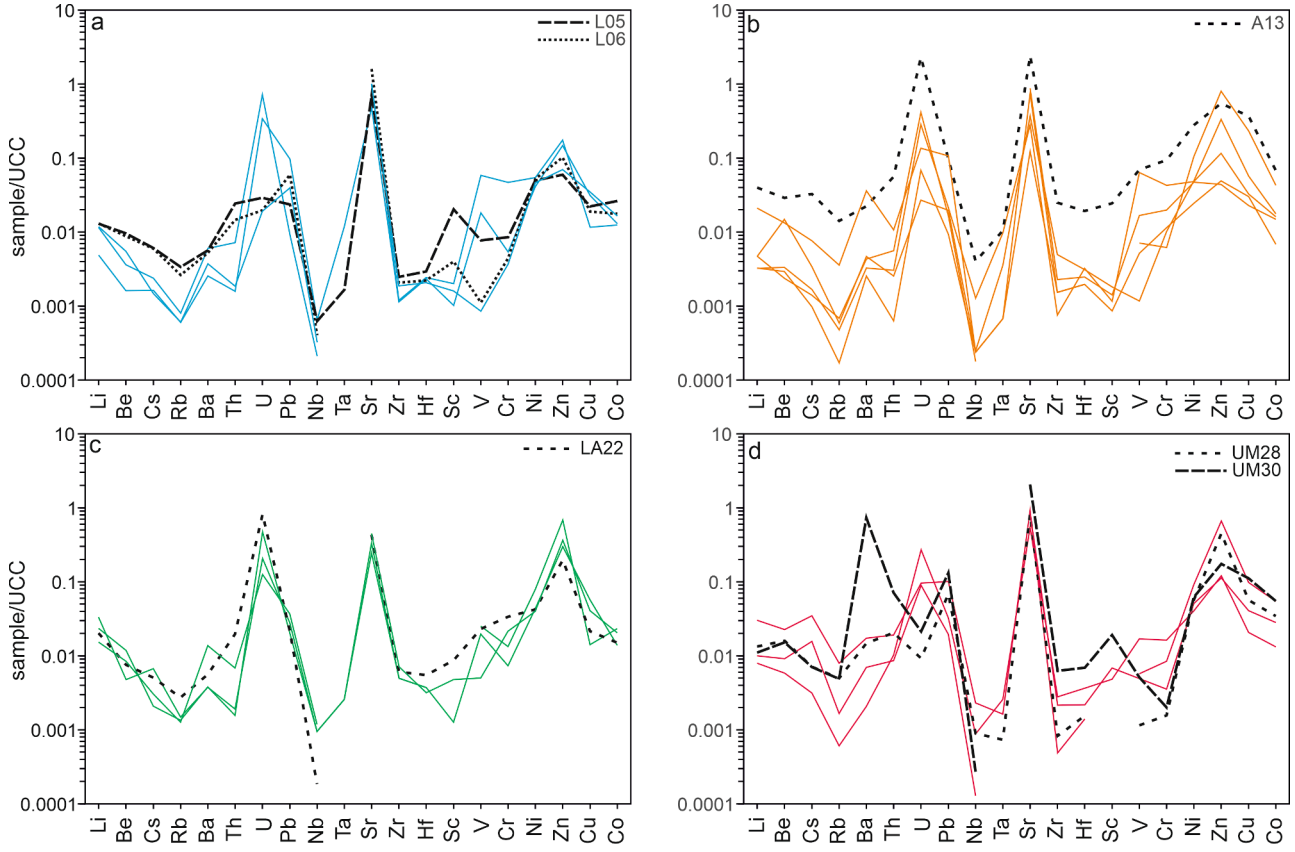

Fig. 5. Limestone' trace elements normalised to Upper Continental Crust (UCC) of McLennan et al. (2001). a) southern area: Lagonegro basin; b) southern area: Apulian platform; c) central area; Lazio-Abruzzo sequence; d) northern area: Umbria-Marche sequence.

peak, while V shows a positive peak but not in all samples (Fig. 5a-d).

3.3. *Rare Earth Elements + Yttrium (REY)*

The limestones have low REE concentrations with ΣREE that range from 0.51 ppm (LA17) to 34.22 ppm (UM30). The Rare Earth Elements + Yttrium (hereafter REY) normalized to PAAS (REY_{PAAS}) show variation of three orders of magnitude (see Fig. 6) and all are depleted relative to PAAS.

The REY_{PAAS} patterns for the limestones display an overall progressive enrichment of heavy REE (HREE) over middle REE (MREE) and light REE (LREE) with La/Yb_{PAAS} ratios generally < 1 with the exception of samples *L*00, L03, and A09 (Table 3). The relative enrichment of HREE over LREE observed is typical of sea-water sediments, and has been attributed to the formation of complexes with CO_3^{2-} and other ligands (Piper and Bau, 2013). Other common features include the negative Ce anomaly (apart from L03, A08, and LA17) and a positive Y anomaly (Fig. 6). In general, appreciable Eu positive anomaly is present only in samples with higher REY concentrations (i.e. L05, A13, A14, UM30) with the only exception of sample LA17 (Fig. 6c). The REY depleted samples, instead, show low $HREE/LREE_{(PAAS)}$ ratios and an uneven $MREE_{PAAS}$ distribution with a small positive Gd anomaly (i.e.

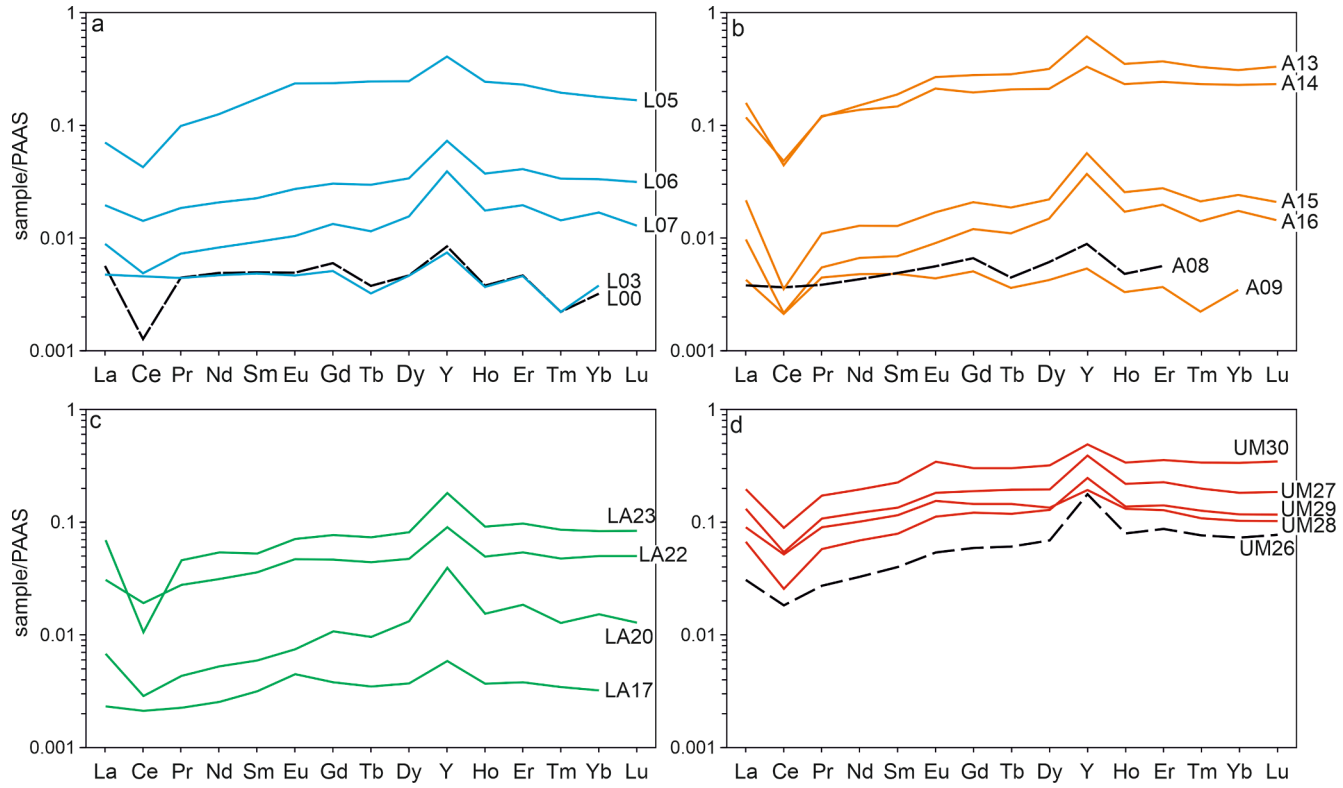

Fig. 6. REY concentrations normalized to PAAS (Pourmand et al., 2012); a) southern section: Lagonegro basin; b) southern section: Apulian platform; c) central section; Lazio-Abruzzo sequence; d) northern section: Umbria-Marche sequence.

L07, L03, *L*00, A08, A09, LA20, Fig. 6).

3.4. Radiogenic isotopes

We assume that the biogenic limestones analysed represent a proxy for the isotopic composition of the oceanic waters (Faure and Mensing, 2005). The assumption is based on the low content of Si, Al, and Fe in the bulk rocks that indicate minor contributions of detrital material, a conclusion supported also by the bulk rock trace element contents as well as the REY patterns.

The $^{87}Sr/^{86}Sr$ values are quite variable, and range from 0.70716 to 0.70809 (Table 4, Fig. 7a). Variation of $^{87}Sr/^{86}Sr$ ratios in limestones, particularly those of Cenozoic age, has been successfully used to obtain numerical dates based solely on their Sr isotopic composition. Comparison of our $^{87}Sr/^{86}Sr$ isotopic ratios with the curves of Burke et al. (1982) and McArthur et al. (2001) show a very good match between the $^{87}Sr/^{86}Sr$ dates and the ages based on stratigraphic relationships (Table 1, Fig. 7). In Fig. 7 are reported data from some spatially-related igneous rocks. These having generally a much higher elemental Sr and Nd content may influence the limestone radiogenic isotope compositions.

The $^{143}Nd/^{144}Nd$ ratios of the limestones analysed in this study range from 0.51191 to 0.51263 (Table 2). The Nd isotopic ratios are variable due the variation in the age as well as the bulk chemistry of the sources that fed into the Tethys ocean. The Nd values for the limestones are much lower than those from the Tethys ophiolites and basalts and the coeval magmatism that occurred within or around the Tethys (Fig. 7b). This is consistent with the influence of crustal input (Lacan et al., 2012; Arsouze et al., 2009; Muiños et. al., 2008) as outlined by the low $^{143}Nd/^{144}Nd$ ratios of the North East Atlantic (NEA) water masses (Fig. 7b), reflecting the silicoclastic input from the surrounding Canada and Greenland continental shields (Muiños et al., 2008).

In addition to Sr and Nd, Pb isotope ratios were also measured. The Pb isotope ratios show a much wider range of values than those of Nd and Sr. $^{206}Pb/^{204}Pb$ spans between 18.59 and 50.92, $^{207}Pb/^{204}Pb$ between 15.66 and 17.18, and $^{208}Pb/^{204}Pb$ from 37.89 and 38.92 (Table 4, Fig. 8).

The $^{206}Pb/^{204}Pb$, $^{207}Pb/^{204}Pb$ and $^{208}Pb/^{204}Pb$ data lie within the limit of the variation field for the Tethys ophiolites and basalts as well as magmatic rocks emplaced in the Mediterranean area in the time span considered. Other than five data points, most define a linear array with a range similar to those obtained from Fe-Mn crusts found in different oceans (Fig. 8) e.g. the North East Atlantic (NEA of Muiños et. al., 2008), the Indian Ocean (IO of Frank and O'Nions, 1998), and the Southern (Antarctic) Ocean (SO from Basak et al., 2011). However, most radiogenic samples, lie away from the linear array (Fig. 8a and 8b). These samples have more radiogenic $^{206}Pb/^{204}Pb$ and $^{207}Pb/^{204}Pb$ isotopic ratios than authigenic ferromanganese coatings of sediments containing a record of the Late Quaternary Mediterranean Outflow Water (MOW of Stumpf et al., 2010) and other oceanic waters whose variations are linked to mass mixing, as well as hydrothermal and detrital inputs (eg. Frank and O'Nions 1998; van de Flierdt et al., 2004; Muiños et. al., 2008).

The anomalous samples (Fig. 8a and 8b) fall into two age groups, one of Lower Jurassic (201–177 My) and the other of Lower Cretaceous (122–118 Ma, Aptian). The Jurassic samples include sample L03 of the southern section and samples LA20, and LA22 of the central section. The two Cretaceous samples are LA17 of the central section and sample A09 of the southern section. These anomalies will be discussed in detail below.

The $^{208}Pb/^{204}Pb$ values of limestones range from 37.9 to 38.9 forming a relatively tight vertical array (see Table 1, Fig. 8c) and are, on the whole, less scattered than the $^{206}Pb/^{204}Pb$ and $^{207}Pb/^{204}Pb$ ratios. The $^{208}Pb/^{204}Pb$ values lie well within the range of variation shown by the Tethys ocean floor rocks and coeval Mediterranean igneous activity. Compared with the Fe-Mn crustal time series, the $^{208}Pb/^{204}Pb$ values of the studied limestone range from the more radiogenic Indian Ocean data that had a contribution from erosion of the uplifting Himalayan

Table 3
Trace elements (ppm).

	L00	L03	L05	L06	L07	A08	A09	A13	A14	A15	A16	LA17	LA20	LA22	LA23	UM26	UM27	UM28	UM29	UM30	LOD[1]	LOQ[2]
Li	0.10	0.23	0.26	0.26	0.24	0.09	0.06	0.80	0.42	0.09	0.06	0.67	0.47	0.41	0.31	0.16	0.60	0.26	0.20	0.22	0.000048	0.000066
Be	0.005	0.011	0.029	0.026	0.016	0.007	0.010	0.087	0.040	0.045	0.009	0.014	0.036	0.023	0.025	0.017	0.068	0.048	0.027	0.045	0.0000022	0.0000103
Cs	0.007	0.011	0.028	0.027	0.007	0.006	0.008	0.149	0.035	0.015	0.004	0.031	0.010	0.023	0.014	0.014	0.159	0.033	0.072	0.032	0.0000235	0.0000487
Rb	0.067	0.090	0.378	0.295	0.068	0.076	0.053	1.582	0.398	0.066	0.019	0.168	0.152	0.308	0.142	0.067	0.890	0.553	0.185	0.546	0.000021	0.0000332
Ba	1.40	3.29	3.12	2.87	2.04	2.36	1.79	12.21	19.77	2.55	1.40	2.07	2.10	3.10	7.55	1.14	9.45	8.03	3.84	400.53	0.0000153	0.0000434
Th	0.017	0.077	0.259	0.155	0.020	0.059	0.032	0.594	0.114	0.027	0.007	0.021	0.017	0.211	0.073	0.109	0.204	0.218	0.092	0.756	0.0000023	0.0000052
U	0.95	2.00	0.08	0.05	0.05	1.16	0.79	6.39	0.38	0.08	0.19	0.58	1.33	2.30	0.35	0.76	0.27	0.03	0.25	0.06	0.0000081	0.0000361
Pb	1.64	0.16	0.40	1.01	0.67	0.28	0.36	1.63	1.82	0.33	0.16	0.48	0.35	0.37	0.63	0.55	1.70	1.15	0.33	2.23	0.0000182	0.0000656
Nb	0.008	0.003	0.008	0.005	0.004	0.002	0.015	0.048	0.003	0.003	0.003	0.011	0.011	0.002	0.014	0.011	0.027	0.011	0.002	0.003	0.000001	0.0000037
Ta	0.012	bdl	0.002	bdl	bdl	bdl	0.010	0.010	0.001	0.004	0.001	0.003	0.003	bdl	0.000	0.003	0.002	0.001	bdl	bdl	0.00005	0.00018
La	0.25	0.21	3.14	0.87	0.40	0.17	0.19	5.24	7.06	0.96	0.43	0.10	0.30	1.37	3.09	1.37	5.89	4.04	2.98	8.75	0.0000003	0.000001
Ce	0.11	0.40	3.76	1.25	0.43	0.32	0.19	4.25	3.90	0.31	0.19	0.19	0.25	1.69	0.93	1.62	4.80	4.57	2.27	7.88	0.0000002	0.0000007
Pr	0.05	0.04	1.00	0.19	0.07	0.04	0.05	1.21	1.23	0.11	0.06	0.02	0.04	0.28	0.46	0.28	1.09	0.92	0.59	1.75	0.0000002	0.0000006
Sr	166.9	351.7	246.1	558.2	350.2	305.9	98.1	838.6	259.5	129.0	42.7	117.4	86.0	151.9	157.8	188.9	321.2	286.1	296.3	720.3	0.0000169	0.0000257
Nd	0.18	0.18	4.67	0.77	0.31	0.16	0.18	5.60	5.11	0.48	0.25	0.09	0.20	1.16	2.01	1.22	4.55	3.79	2.58	7.30	0.000001	0.0000037
Zr	0.22	0.23	0.47	0.39	0.35	0.43	0.14	4.69	0.29	0.94	0.29	0.95	0.95	1.16	1.35	0.53	0.09	0.16	0.41	1.19	0.00016	0.0005
Hf	0.013	0.014	0.017	0.013	0.012	0.014	0.019	0.111	0.011	0.018	0.011	0.022	0.022	0.032	0.019	0.021	0.008	0.009	0.013	0.040	0.00054	0.00154
Sm	0.034	0.033	1.182	0.155	0.064	0.034	0.033	1.290	1.010	0.088	0.048	0.022	0.041	0.247	0.363	0.276	0.929	0.798	0.545	1.552	0.0000017	0.0000056
Eu	0.006	0.006	0.286	0.033	0.013	0.007	0.005	0.326	0.257	0.021	0.011	0.005	0.009	0.057	0.086	0.066	0.222	0.188	0.136	0.419	0.000001	0.0000033
Gd	0.036	0.031	1.430	0.183	0.080	0.040	0.031	1.681	1.180	0.125	0.073	0.023	0.065	0.280	0.463	0.357	1.140	0.877	0.733	1.830	0.0000007	0.0000036
Tb	0.003	0.003	0.218	0.026	0.010	0.004	0.003	0.253	0.186	0.017	0.010	0.003	0.008	0.039	0.065	0.054	0.174	0.129	0.106	0.269	0.0000002	0.0000015
Dy	0.025	0.025	1.313	0.180	0.083	0.032	0.023	1.681	1.119	0.117	0.079	0.020	0.070	0.251	0.433	0.367	1.040	0.716	0.686	1.700	0.0000002	0.0000025
Y	0.230	0.204	11.113	1.988	1.070	0.242	0.146	16.737	9.055	1.545	1.009	0.160	1.073	2.454	4.943	4.845	10.683	5.288	6.748	13.430	0.00005	0.00017
Ho	0.004	0.004	0.256	0.039	0.018	0.005	0.003	0.369	0.245	0.027	0.018	0.004	0.016	0.052	0.096	0.084	0.231	0.139	0.146	0.357	0	0.0000005
Er	0.014	0.014	0.708	0.126	0.060	0.017	0.011	1.136	0.748	0.085	0.061	0.012	0.057	0.166	0.298	0.268	0.698	0.394	0.434	1.097	0.0000003	0.000002
Tm	bdl	bdl	0.088	0.015	0.006	0.001	bdl	0.149	0.105	0.010	0.006	0.002	0.006	0.021	0.039	0.035	0.090	0.049	0.057	0.153	0.0000001	0.0000009
Yb	0.010	0.011	0.540	0.100	0.051	0.015	0.010	0.929	0.689	0.072	0.052	0.010	0.046	0.150	0.251	0.220	0.548	0.310	0.354	1.017	0.0000014	0.0000047
Lu	bdl	bdl	0.073	0.014	0.006	0.001	0.0002	0.145	0.102	0.009	0.006	0.002	0.006	0.022	0.037	0.034	0.082	0.045	0.051	0.152	0.000001	0.0000031
Sc	0.051	0.100	1.016	0.200	0.079	0.070	0.058	1.218	na	0.091	0.043	na	0.064	0.436	0.240	0.240	na	na	0.340	0.951	0.0000141	0.0000524
V	1.937	6.210	0.828	0.119	0.091	1.775	6.774	7.381	0.760	0.124	0.551	2.697	2.115	2.477	0.537	1.806	0.608	0.122	0.527	0.547	0.0000359	0.0000908
Cr	0.447	3.883	0.704	0.367	0.306	1.631	3.522	7.786	0.510	0.843	0.946	1.110	0.610	2.806	1.798	1.351	0.698	0.130	0.292	0.166	0.0000174	0.0000985
Cd	0.049	0.062	0.023	0.038	0.035	0.029	0.039	0.125	0.226	0.040	0.071	0.033	0.059	0.107	0.181	0.056	0.190	0.134	0.011	0.180	0.0000036	0.0000129
Ni	1.80	2.38	2.18	2.29	2.04	2.06	2.10	12.22	4.59	2.14	1.08	3.46	1.91	1.88	1.76	1.77	3.99	2.49	2.22	2.72	0.0000023	0.0000227
Zn	2.49	2.97	1.01	1.73	1.18	0.74	1.95	9.23	13.54	5.62	0.83	11.65	5.08	3.37	6.22	2.05	11.22	7.62	1.90	2.96	0.000002	0.0004355
Cu	0.78	0.29	0.55	0.47	0.87	0.57	0.81	9.13	5.81	1.42	0.75	0.35	1.44	0.54	1.02	0.52	2.44	1.40	1.02	2.78	0.0000036	0.0002702
Co	0.22	0.21	0.45	0.30	0.28	0.25	0.27	1.14	0.72	0.30	0.12	0.40	0.24	0.26	0.35	0.22	0.92	0.58	0.48	0.93	0.0000106	0.000023
ΣREE	0.73	0.96	18.67	3.96	1.60	24.25	1.29	0.72	0.85	2.43	22.94	8.62	0.51	5.79	1.12	6.25	21.48	16.96	11.67	34.22		
La/Yb_{PAAS}	1.77	1.25	0.39	0.59	0.53	0.38	0.56	1.23	0.79	0.90	0.69	0.83	0.72	0.62	0.45	0.42	0.73	0.88	0.57	0.58		
Y/Ho	57.7	52.5	43.4	50.4	58.0	47.9	41.9	45.3	37.0	57.6	56.1	41.3	66.5	47.2	51.6	57.8	46.2	38.1	46.4	37.6		
La/Ce_{PAAS}	4.5	1.0	1.7	1.4	1.8	2.4	4.5	2.0	1.0	6.1	3.6	6.6	1.1	1.6	2.4	1.7	2.4	1.7	2.6	2.2		
Sr/Rb	2476	3923	650	1892	5143	4024	1853	530	651	1964	2250	700	567	493	1111	2799	361	517	1604	1319		
Sr/Ba	119.3	106.8	78.9	194.2	171.3	129.5	54.9	68.7	13.1	50.6	30.5	56.8	41.0	49.0	20.9	166.1	34.0	35.6	77.2	1.8		
Sm/Yb_{PAAS}	1.55	1.28	0.96	0.68	0.55	0.61	0.40	1.39	1.01	0.53	0.64	0.63	0.98	0.72	0.39	0.55	0.74	1.13	0.67	0.67		
Ce/Ce*	0.24	0.97	0.48	0.71	0.56	0.37	0.25	0.48	0.92	0.19	0.29	0.16	0.88	0.62	0.46	0.58	0.42	0.55	0.38	0.46		
V/Cr	4.33	1.60	1.18	0.32	0.30	1.09	1.92	0.95	1.49	0.15	0.58	2.43	3.47	0.88	0.30	1.34	0.87	0.94	1.81	3.30		

[1] - limit of detection (LOD) [2] -limit of quantification (LOQ). Both were calculated for all elements by analysing ten experimental blanks:$y_{LOD} = yb + 3s_b$;$y_{LOQ} = yb + 10s_b$. Where yb is the average blank signal and s_b is the standard deviation of the blank signal. The corresponding concentration values were obtained by using an appropriate calibration curve satisfying the following relationship: $0.5x_1 < LOD < x_1$, where x_1 is the concentration of the first calibration level. na = not analysed; bdl = below detection limits.

Table 4
Radiogenic isotopes.

	Sample	$^{87}Sr/^{86}Sr$		2	$^{143}Nd/^{144}Nd$		2	$^{206}Pb/^{204}Pb$		2	$^{207}Pb/^{204}Pb$		2	$^{208}Pb/^{204}Pb$		2
southern area	L00	0.707440	±	4	0.51230	±	9	18.64	±	0.01	15.67	±	0.01	38.43	±	0.01
	L03	0.707310	±	2	0.51222	±	7	32.47	±	0.01	16.35	±	0.03	38.92	±	0.01
	L05	0.707820	±	6	0.51238	±	8	19.89	±	0.01	15.71	±	0.01	38.84	±	0.02
	L06	0.708070	±	3	0.51222	±	10	18.59	±	0.02	15.66	±	0.01	38.64	±	0.01
	L07	0.708030	±	5	0.51211	±	11	18.81	±	0.01	15.68	±	0.01	38.77	±	0.04
	A08	0.707320	±	5	0.51220	±	2	20.20	±	0.01	15.7	±	0.02	37.89	±	0.01
	A09	0.707440	±	3	0.51230	±	7	50.92	±	0.03	17.18	±	0.01	38.62	±	0.01
	A13	0.708810	±	4	0.51224	±	9	19.05	±	0.01	15.67	±	0.01	38.53	±	0.01
	A14	0.707000	±	2	0.51236	±	9	21.32	±	0.01	15.78	±	0.01	38.61	±	0.01
	A15	0.707160	±	2	0.51233	±	9	18.94	±	0.01	15.67	±	0.01	38.73	±	0.02
	A16	0.707910	±	6	0.51230	±	6	20.39	±	0.01	15.73	±	0.01	38.69	±	0.01
central area	AL217	0.707380	±	4	0.51217	±	10	26.18	±	0.01	16.03	±	0.01	38.68	±	0.01
	AL20	0.707650	±	6	0.51231	±	9	37.37	±	0.01	16.6	±	0.01	38.84	±	0.01
	AL22	0.707300	±	1	0.51216	±	11	32.78	±	0.01	16.37	±	0.01	38.85	±	0.01
	AL23	0.707700	±	2	0.51224	±	8	19.19	±	0.01	15.68	±	0.01	38.64	±	0.01
northern area	UM26	0.707580	±	3	0.51230	±	8	19.01	±	0.01	15.89	±	0.01	38.76	±	0.03
	UM27	0.707350	±	7	0.51223	±	6	18.76	±	0.01	15.7	±	0.01	38.9	±	0.01
	UM28	0.707220	±	4	0.51227	±	9	18.69	±	0.01	15.66	±	0.02	38.95	±	0.01
	UM29	0.707360	±	6	0.51222	±	9	19.39	±	0.01	15.69	±	0.01	38.69	±	0.02
	UM30	0.707700	±	5	0.51228	±	9	18.73	±	0.01	15.68	±	0.01	38.89	±	0.01

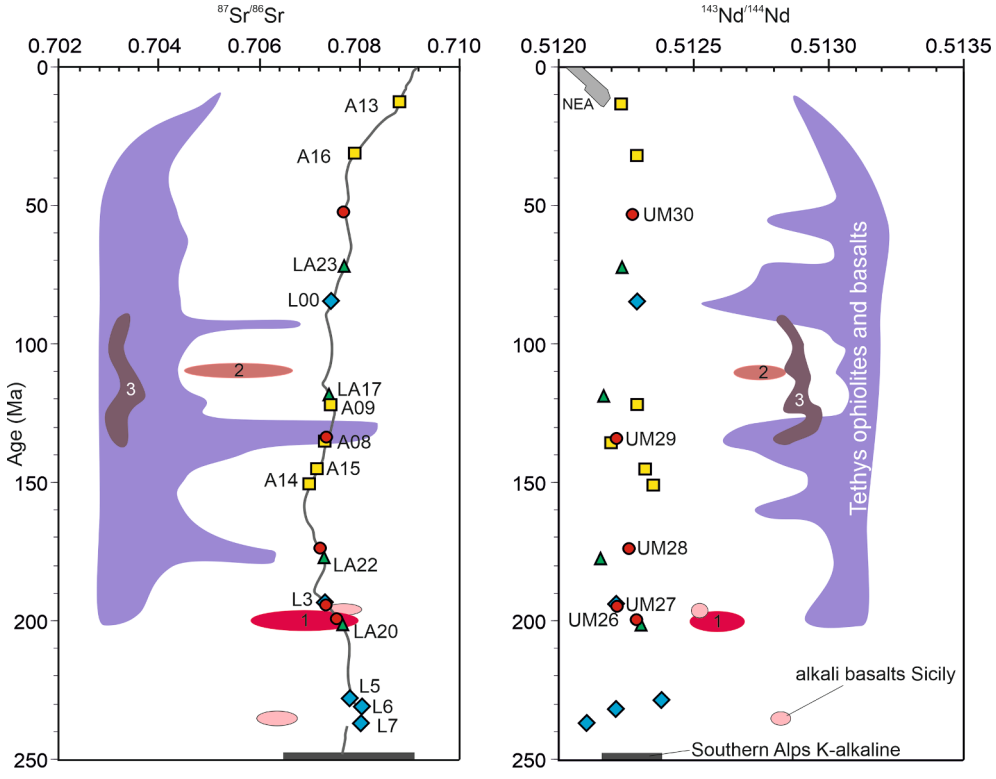

Fig. 7. (A) sr isotopic ratios and the chronostratigraphic curve (thick black line) based on data from Burke et al. (1982) and McArthur et al. (2001); b) Nd isotopic ratio variation with stratigraphic age. The comparison with regional magmatic phases can give a measure of the composition of magmatic fluids/detritus possibly influencing carbonate composition. The grey areas represent the data from Tethys ophiolites and basaltic lavas (Chen and Pallister, 1981; Mahoney et al., 1998; Xu and Castillo, 2004; Zhang et al., 2005), the alkali basalts from Sicily data are from Cirrincione et al. (2014), Cirrincione et al. (2015). Other magmatic rocks: 1 - Portugal-Spain doleritic dykes, from Cebrià et al. (2003), 2 - Senna River (Tuscany) lamprophyres from Stoppa et al. (2014), 3 - Mt Hermon, (Northern Israel) from Wilson et al. (2000). 4 - Southern Alps (high-K calc-alkaline magmatism) from Rottura et al. (1998). NEA – North East Atlantic (Muiños et. al., 2008). Limestone color legend as Fig. 3.

mountains (Frank and O'Nions, 1998) and the less radiogenic data of Baur Basin whose large variation is linked to the reduction of hydrothermal input of the Galapagos Rise spreading center (van de Flierdt et al., 2004). The anomalously low $^{208}Pb/^{204}Pb$ ratio of sample A08 (Fig. 8c) might be consistent with a dominant hydrothermal input into the ocean waters. Other chemical features of A08 include low Zn, La, and Zr, and a lack of negative Ce anomaly.

4. Discussion

Limestones show general negative correlations between CaO and SiO_2, Al_2O_3, and Fe_2O_3 (Fig. 3) indicating that Ca in the carbonates is of biogenic origin (Zhang et al., 2017). The low abundance of Al_2O_3 (e.g. < 0.42 wt%; Veizer 1983) and Fe_2O_3, their good positive correlation (R^2 values above 0.9, Fig. 4a) along with the weak correlation between Al_2O_3 and MnO (Fig. 4b), suggests that the limestones formed at distance from the continents (Zhang et al., 2017), with little contamination from terrestrial particulate matter (i.e. clay) (Madhavaraju et al., 2016). This is supported also by the low content in Th and Zr, as well as the lack of any correlation between ΣREE and Al_2O_3, which indicates little contribution of detrital terrigenous particulate material (i.e. shale) to the bulk of the limestones (Madhavaraju et al., 2016).

The analysed limestones show broad variations of REY_{PAAS} patterns within almost three orders of magnitude and general enrichment of HREE relative to the LREE accompanied by a positive Y spike (Fig. 6). These geochemical features are in keeping with typical seawater-like REY patterns (Tostevinet et al., 2016, Piper and Bau, 2013, Madhavaraju and González-León, 2012) suggesting that the REY concentrations

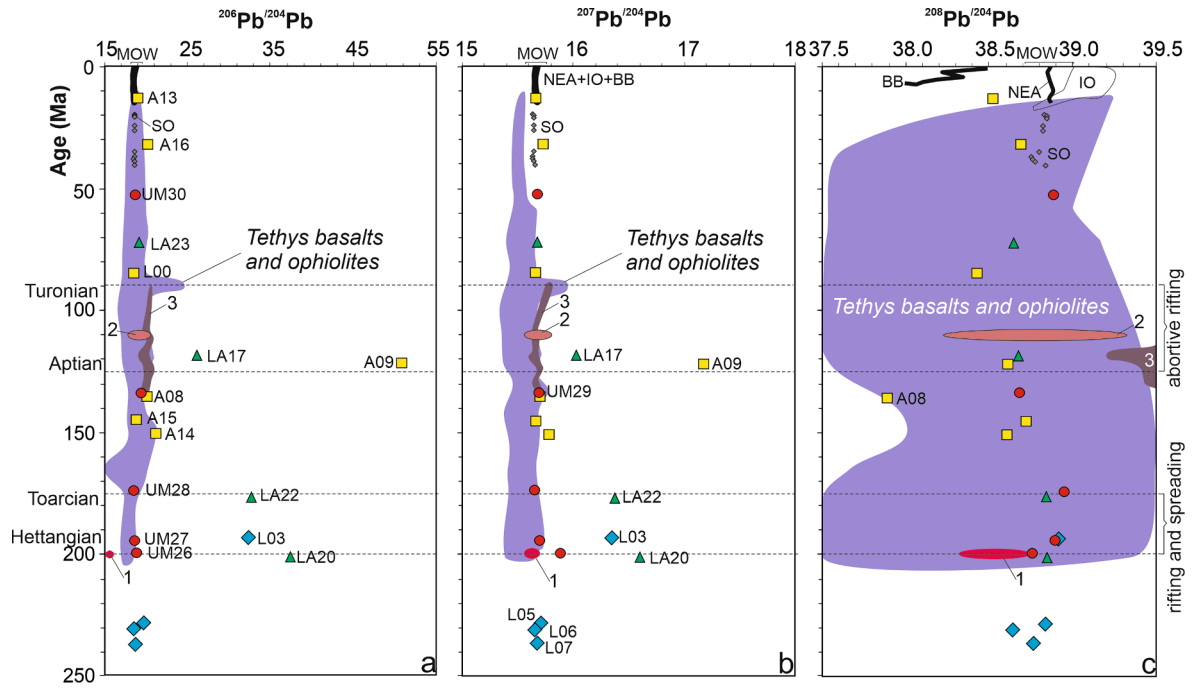

Fig. 8. Comparison of Pb isotope ratios of limestones vs ages. a) $^{206}Pb/^{204}Pb$ vs age; b) $^{207}Pb/^{204}Pb$ vs age, c) $^{208}Pb/^{204}Pb$ vs age. There are minor perturbations of the $^{206}Pb/^{204}Pb$ and $^{207}Pb/^{204}Pb$ ratios (samples L03, LA20, LA22) in the time span of 201–177 Ma (Early Jurassic). Similar anomalous $^{206}Pb/^{204}Pb$ and $^{207}Pb/^{204}Pb$ ratios (samples LA17 and A09) within the time span of 122–118 (Aptian) upper part of the Lower Cretaceous. In gray are reported the data compilation of ophiolites plus basalts of the Tethyan seafloor (Chen and Pallister, 1981; Mahoney et al., 1998; Xu and Castillo, 2004; Zhang et al., 2005). Tethyan igneous activity: 1 - Portugal-Spain doleritic dykes, from Cebrià et al. (2003); 2 – Senna River (Tuscany) lamprophyres from Stoppa et al. (2014); 3 - Mt Hermon, (Northern Israel) from Wilson et al. (2000). Fe-Mn crustal time series: IO - Indian Ocean (Frank and O'Nions, 1998), NEA – North East Atlantic (Muiños et. al., 2008); SO - Southern Ocean (Basak et al., 2011); BB -Baur Basin (van de Flierdt et al., 2004); MOW - Late Quaternary Mediterranean Outflow Water (Stumpf et al., 2010). Limestone color legend as Fig. 3.

were mainly derived from seawater. The REY_{PAAS} patterns (see Fig. 6) show very weak Eu-positive anomalies in samples UM30, A13, L05, and the general low Eu/Eu* ratios ranging from 0.40 to 0.49 (Table 3) might indicate a very limited input of hydrothermal fluids into seawaters since Eu sources of this type are mainly related to high-temperature, magmatic activity (Nagarajan et al., 2011). In marine limestones,

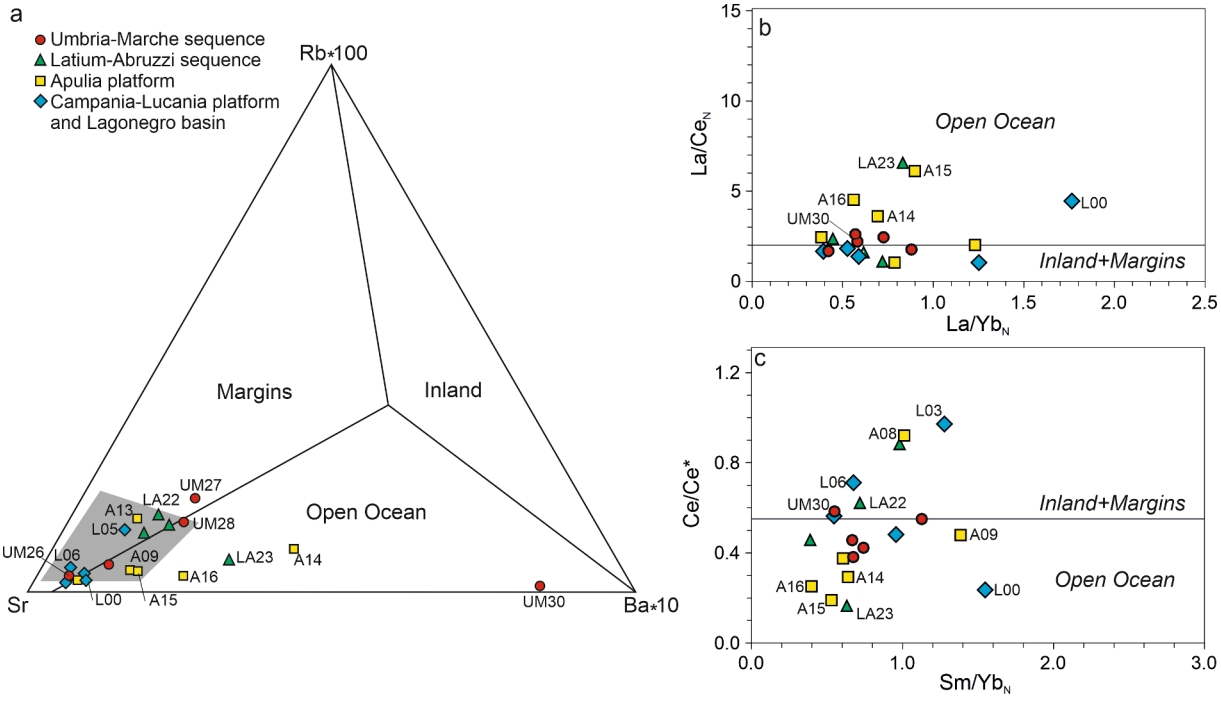

Fig. 9. (A) sr-ba-rb diagram of Zhang et al. (2017). The gray area represents the limestones of the *meso*-Tethyan oceanic plateaux in Tibet (Zhang et al., 2017); b) La/Yb_N vs La/Ce_N and Sm/Yb_N vs Ce/Ce* of analysed limestones in the plate tectonic depositional setting framework defined by Zhang et al., (2017).

positive Y anomalies are produced by fractionation of LREE, MREE, and HREE on organic and inorganic particulate surfaces (Piper and Bau, 2013). In particular, phosphatized crusts produce Y enrichments in seawaters (Bau et al., 1996). The Y/Ho ratio variation from 37.6 to 66.5, well above the chondritic value of 28 (Bau et al., 1996), indicates that the contribution from terrigenous sediments to the overall REY budget was small.

The Italian limestone Y/Ho ratios varying from 37 to 66.5 (Table 3), fall within the range of the *meso*-Tethyan oceanic plateau limestones of Zhang et al. (2017). The range of Sr abundances (Table 3) is within the normal seawater limestones variation interval (Zhang et al., 2017). Thus, we use the Rb-Sr-Ba diagram proposed by Zhang et al. (2017) for discriminating the tectonic setting of our limestones. Most samples fall into the Ocean Margin field or very close to the Margin-Open ocean divide (Fig. 9a). However, samples A14, A15, A16, LA23, and UM30 fall within the Open Ocean field (Fig. 9a). Sample UM30, with its high Ba content, (Table 3), plot close to the Open Ocean-Inland divide and is clearly anomalous. This sample, however, belongs to the "Scaglia Rossa Formation" (SAA in Fig. 2) representing a pelagic succession with stratified calcareous fractions dominating over variable amounts of marl. Considering the PAAS normalized, mobile element ratios such as La/Yb_N vs La/Ce_N are evident the consistency of the depositional regime as oceanic and of continental margin (Fig. 9b). It is also supported by the coupled high Sr/Rb and Sr/Ba ratios along with low immobile elements content like Nb, Ta, Zr, and Hf (Fig. 5). However, considering Sm/Yb_N vs Ce/Ce* (Fig. 8b) the low Ce/Ce* ratios of the A14, A15, A16, LA23 samples indicate a depositional environment of open ocean, while sample UM30 lies within the inland + margins field (Fig. 9b and 9c).

The samples have Ce/Ce* ratios < 1 (Lawrence et al., 2006) indicating limestone formation in well-oxygenated seawater (Shields and Stille, 2001; Pourmand et al., 2012). Insights into the fO_2 for the assessment of the paleo-oxygenation of seawater can be also obtained using V/Cr ratios (Madhavaraju et al., 2016). The sample set analysed have V/Cr ratios mostly below 2, indicating carbonate deposition in oxygenated waters. Sample LA20 and UM30 have a V/Cr ratio between 2 and 4 indicating a sub-oxic formation condition and sample *L*00 has a V/Cr ratio of 4.33 suggesting an anoxic condition (Fig. 9). The variation of water oxygenation does not correlate with Pb radiogenic isotopic variations (Fig. 10).

Noteworthy, the data from the Italian Tethys fall close to those of the *meso*-Tethyan oceanic plateau in Tibet (Zhang et al., 2017), suggesting that the oceanic waters in the Mediterranean and Himalaya Tethys were connected (Fig. 9a). The reasonable agreement between the Sr dates for the analysed limestones and the stratigraphic ages indicates that

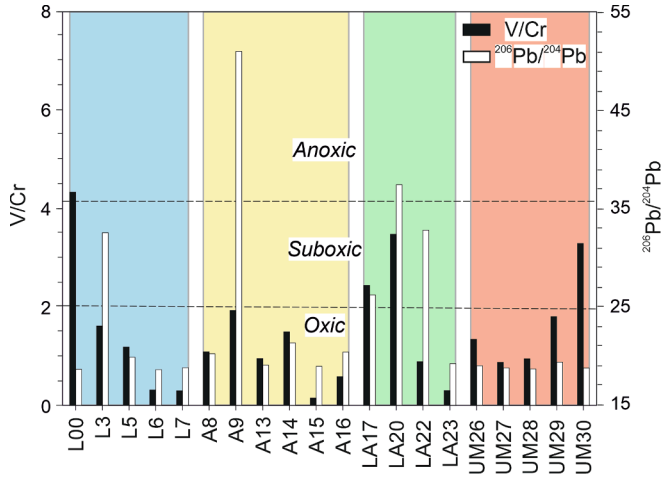

Fig. 10. Variation of V/Cr ratios indicating seawater paleoenvironmental conditions of limestone deposition compared with the variation of $^{206}Pb/^{204}Pb$ isotopic ratios.

throughout history, a period of at least 230 Ma, the central Mediterranean portion of the Tethys was part of the ocean's global circulation. In summary, the major and trace element as well as REY data show patterns similar to those of limestones from elsewhere, reflecting deposition in well-oxygenated seawater and a low contribution from detrital terrigenous sediments and hydrothermal activity.

Trace metals with distinct radiogenic isotope compositions (Sr, Nd, Pb, Os, Hf) in seawater reflect riverine and/or eolian inputs (crustal signal), as well as hydrothermal activity (seafloor spreading signal) since these isotope ratios, are also "independent from fractionation induced by biological process or evaporation" (Frank, 2002). Any variations in isotope composition, therefore, reflect mixing between water masses with different isotopic compositions, which in turn are linked to climate and crustal geodynamic evolutions.

The $^{87}Sr/^{86}Sr$ isotopic ratios in the limestones analysed are relatively restricted and reasonably match the stratigraphic ages, thus appears that the Sr isotopic compositions have remained unaffected during diagenesis, burial or tectonic exhumation. It implies that limestone $^{87}Sr/^{86}Sr$ isotopic ratios did not record major crustal input events from either the African or the European continents during the evolution of the Tethys ocean.

However, the Sr and Pb isotopic composition recorded in the limestone, which reflects the isotopic composition of oceanic water masses, may differ from the crustal source because during the weathering of continental rocks, radiogenic Pb and Sr isotopes can be preferentially released (Erel et al., 1994; Silver et al., 1984) during physical erosion (von Blanckenburg and Nägler, 2001; Frank, 2002).

The residence time of Sr in seawater is of the same order of magnitude as the global oceanic stirring time i.e. 2.4 Ma (McArthur et al., 2001), resulting in efficient mixing of water masses with different Sr isotope signatures. In contrast, Pb and Nd have much shorter residence times. Pb residence time is ~ 50–200 yrs (Henderson and Maier-Reimer, 2002) shorter than Nd residence time which is in the order of 300 to 1000 yrs (Lacan et al., 2012; Noble et al., 2015). It implies that Pb and Nd isotopic ratios can vary not only within the major oceans but can also vary from one basin to another (e.g. Frank, 2002; Lacan et al., 2012), thus can be used as tracers of their source, past oceanic circulation, and climate (eg. Abouchami and Goldstein, 1995; Muiños et al., 2008; Lacan et al., 2012; Dera et al., 2015). The Jurassic samples, LA22 and UM28, have similar Nd isotopic ratios of coeval *peri*-Tethyan seas of Dera et al. (2015), suggesting again the Tethyan basin' interconnection.

The Italian limestones have been continuously deposited in different environments throughout the Cenozoic in response to the evolution of the neoTethys basins. Because of the short residence time of Pb in oceans, it is sensitive to any input from the continental crust. The most radiogenic samples (see Fig. 8) fall within two quite narrow time intervals. Samples L03, LA20, and LA22 are of Lower Jurassic (201–177 Ma), while samples A09 and LA17 are of Lower Cretaceous age (122–118 Ma, Aptian). These high $^{206}Pb/^{204}Pb$ and $^{207}Pb/^{204}Pb$ ratios might reflect the input of Pb into the ocean basins from high U/Pb sources (e.g. Frank, 2002). The input might be related to changes in weathering regime due to major geodynamic events and/or climate changes. The latter hypothesis can be excluded because there were no major deglaciation episodes during Lower Jurassic and Lower Cretaceous (Veizer et al., 1999; Veizer et al., 2000).

In the time interval between 210 Ma and 185 Ma, rifting and spreading have been linked to the breakup of Pangea affecting those areas between Africa and Europe. The rifting separated Spain from Morocco and Tunisia and generated the Ionian ocean (composed of the Lagonegro and Apulia basins) that was once part of the southernmost branch of the NeoTethys. In the north, another branch of the NeoTethys, the Ligurian basin was bordered by rift structures in Tuscany-Umbria-Marche, that started to form at about 200 Ma (Stampfli and Borel, 2002; Raulin et al., 2011; Schettino and Turco, 2011 and references therein). Lower Jurassic limestones of the southern (L03) and central sections (LA20, LA22), were deposited into the Ionian basin. The

anomalous high radiogenic ^{206}Pb and ^{207}Pb can be correlated to this phase of strong physical weathering of old continental rocks (von Blanckenburg and Nägler, 2001). The almost coeval limestone samples of the northern sections (UM26, UM27, UM28) have low radiogenic Pb isotopic ratios suggesting that in the case of the Ligurian basin the continental input was low and/or the water mixing was more efficient. Paleo-geographic reconstructions effectively indicate that the Ligurian and Ionian basins were separated by the Panormide platform (Stampfli and Borel, 2002; Schettino and Turco, 2011) that prevented efficient water mass mixing, at least in the time scale of the Pb residence time.

Samples A09 and LA17 of Aptian age (Lower Cretaceous 122–118 Ma) have very radiogenic Pb ratios perhaps reflecting another major geodynamic event. During the Aptian, the southern NeoTethys area started to develop a divergent movement between Africa and Adria (Stampfli and Borel, 2002; Tavani et al., 2013). This rifting episode initially affected the north African margin and subsequent northward migration during the upper Cretaceous and Eocene reaching the Apennine platforms and the Lagonegro and Abruzzo basins (Vitale et al., 2017 and reference therein). This reactivation of divergent geodynamics was accompanied by widespread anorogenic magmatism (see Vitale et al., 2017 and references therein). Rifting reprisal might have triggered extensive weathering of African continental terrains (Ahfaf et al., 2021) releasing Pb in the southern/central Tethys water masses (Fig. 11). The Pb brought in solution had high $^{206}Pb/^{204}Pb$ and $^{207}Pb/^{204}Pb$ isotopic ratios. This crustal input produced a variation of the isotopic composition of the Tethys water masses and because of the short residence time of Pb, anomalous $^{206}Pb/^{204}Pb$ and $^{207}Pb/^{204}Pb$ ratios were recorded only in the biogenic limestones formed in relatively closed basins. This might indicate sudden and time-limited geodynamic phases not recorded by Sr and Nd isotopic systematics.

Finally, the presence in the peninsular Italy of igneous carbonatite rocks associated with kamafugites and leucitites (see Stoppa et al., 2019 for references) and carbonate in mantle xenoliths (Rosatelli et al., 2007) sparked a lively debate on the involvement of limestones in the Cenozoic magmatism (Bell et al., 2013; Conticelli et al., 2015). Thus, the limestone database compiled is used to define the average, present-day, isotope ratios for the Italian limestones (AIL = average Italian limestone). Excluding anomalous radiogenic samples, AIL average is $^{87}Sr/^{86}Sr$ = 0.707852, $^{143}Nd/^{144}Nd$ = 0.512274, and $^{206}Pb/^{204}Pb$ = 18.94, $^{207}Pb/^{204}Pb$ = 15.69, $^{208}Pb/^{204}Pb$ = 38.66. Such values along, with the element data, can be used for modelling the petrogenesis of the Italian and the *peri*-Tethyan carbonatites and mafic alkaline rocks (Stoppa et al., 2019).

5. Conclusions

The new data from Italian limestones represent a discontinuous time series from Upper Triassic to Miocene. They have major elements composition and trace element contents, in particular REY_{PAAS} patterns, with general enrichment of HREE and MREE over LREE, negative Ce and positive Y anomalies, consistent with "seawater-like" patterns (Piper and Bau, 2013). Therefore, the limestones incorporated elements dissolved in seawater, with negligible input from hydrothermal fluids or terrigenous detrital materials.

The depth of the depositional environment was responsible for the REY budget in the seawaters and limestone. The classification based on Rb-Sr-Ba content and immobile element (HFSE) distribution, of the carbonates, show the paleo-environmental conditions of the Italian limestones (Zhang et al., 2017). It is also interesting that the data from the Italian Tethys limestones fall close to those of the *meso*-Tethyan oceanic plateaux in Tibet (Zhang et al., 2017), and suggest a geographical link between the two basins. The redox conditions through the entire limestone sample set indicates deposition in oxic and sub-oxic environment.

The stratigraphic age of the limestones studied fits the $^{87}Sr/^{86}Sr$ chronostratigraphic curve of McArthur et al. (2001) implying that the neoTethys basins were connected and that the Tethys basins were not isolated from the global ocean system. The $^{143}Nd/^{144}Nd$ ratios of the Italian limestone are much lower than the Tethys ophiolites and basalts indicating important contributions of Nd to water masses during the weathering of continental crustal terrains. Anomalous high $^{206}Pb/^{204}Pb$ and $^{207}Pb/^{204}Pb$ isotopic ratios indicate that were periods of crustal input into the basins during the Lower Jurassic and Lower Cretaceous not coupled, however, with Sr or Nd isotopic ratios variations. It implies a localized effect of crustal input possibly caused by rifting episodes.

The average, present-day, isotope ratios (AIL = Average Italian Limestone) for the Italian limestones based on our sample set excluding anomalous samples, are $^{87}Sr/^{86}Sr$ = 0.707852, $^{143}Nd/^{144}Nd$ =

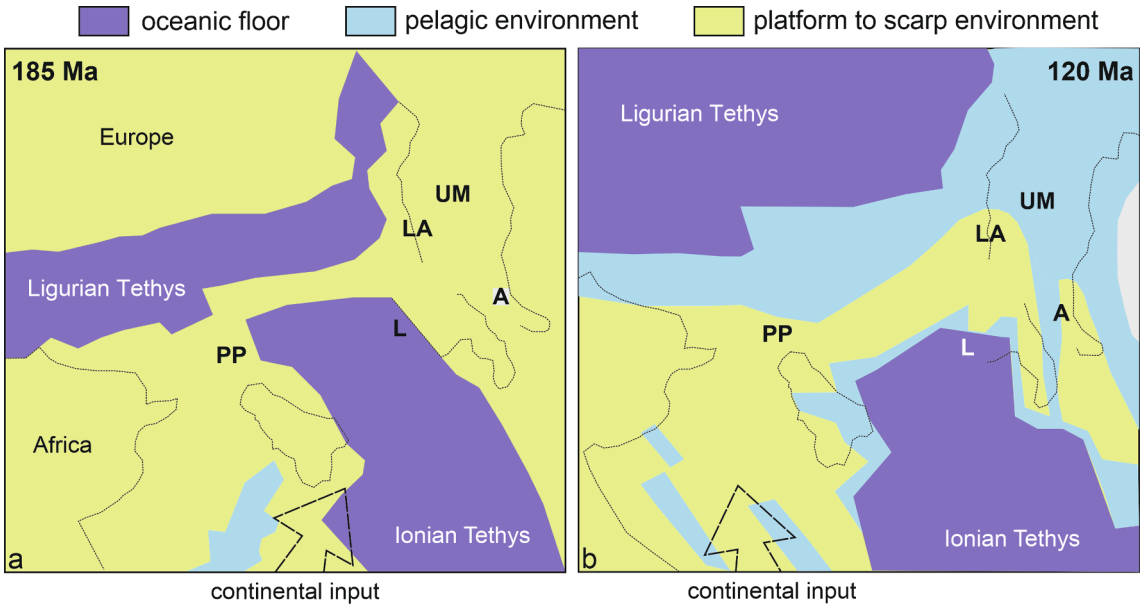

Fig. 11. Schematic paleogeographic reconstruction of the central Mediterranean area during: a) Toarcian, Lower Jurassic (185 Ma); b) Aptian, Lower Cretaceous (120 Ma). UM = Umbria-Marche limestone series, LA = Lazio.Abruzzo limestone series; A = Apulian platform, L = Lagonegro basin; PP = Panormide Platform. Redraw after Stampfli and Borel (2002); Zarcone et al. (2010); Tavani et al. (2013); Vitale et al. (2017).

0.512274, and $^{206}Pb/^{204}Pb = 18.94$, $^{207}Pb/^{204}Pb = 15.69$, $^{208}Pb/^{204}Pb = 38.66$. Such values, along with the element data, are useful as tracers in monitoring the involvement of limestones in Italy during Cenozoic magmatism.

CRediT authorship contribution statement

Rosatelli Gianluigi: Conceptualization, Writing – original draft, Writing – review & editing, Visualization, Formal analysis, Supervision. **Castorina Francesca:** Writing – original draft, Validation, Formal analysis, Investigation. **Consalvo Ada:** Validation, Formal analysis, Investigation. **Brozzetti Francesco:** Formal analysis, Investigation, Writing – review & editing. **Ciavardelli Domenico:** Validation. **Perna Maria Grazia:** Validation, Formal analysis, Writing – review & editing. **Bell Keith:** Writing – original draft, Validation, Formal analysis, Investigation. **Bello Simone:** . **Stoppa Francesco:** Supervision.

Declaration of Competing Interest

The authors declare that they have no known competing financial interests or personal relationships that could have appeared to influence the work reported in this paper.

Data availability

The data used are reported in the paper

Acknowledgments

The Authors would thank Prof. John McArthur for kindly providing the limestone $^{87}Sr/^{86}Sr$ chronostratigraphic database and allowing us to use it. The research was funded by the Department of Disputer - University G. d'Annunzio. The Authors would like to thank Editor Prof. Ibrahim Uysal, Prof. Kai-Jun Zhang, and another anonymous reviewer for the precious comments that helped to improve the manuscript.

References

Abouchami, W., Goldstein, S., 1995. A lead isotopic study of circum-Antarctic manganese nodules. Geochim. Cosmochim. Acta 59, 1809–1820.

Ahfaf, M.M.A., Adepehin, E.J., Ali, C.A., Jamil, H., Lubi, S.P., 2021. Controls on the compositional framework and petrogenesis of Early Cretaceous first cycle quartzose sandstone, North Gondwana. Sediment. Geol. 424, 105982 https://doi.org/10.1016/j.sedgeo.2021.105982.

Arsouze, T., Dutay, J., Lacan, F., Jeandel, C., 2009. Reconstructing the Nd oceanic cycle using a coupled dynamical–biogeochemical model. Biogeosciences 6, 2829–2846. https://doi.org/10.5194/bg-6-2829-2009.

Barchi, M. Bernasconi, A. Brozzetti, F. Lavecchia, G. Menichetti, M. Minelli, G. Nardon, S. Pialli, G., 1993 Joint distribution in a fractured carbonate reservoir in the Umbria-Marche anticlines (Central Italy). In: Spencer, A.M. (eds) Generation, Accumulation and Production of Europe's Hydrocarbons III. Special Publication of the European Association of Petroleum Geoscientists, vol 3. Springer, Berlin, Heidelberg. 10.1007/978-3-642-77859-9_17.

Basak, C., Martin, E.E., Kamenov, G.D., 2011. Seawater Pb isotopes extracted from Cenozoic marine sediments. Chem. Geol. 286, 94–108.

Bau, M., Koschinsky, A., Dulski, P., Hein, J.R., 1996. Comparison of the partitioning behaviors of yttrium, rare earth elements, and titanium between hydrogenetic marine ferromanganese crusts and seawater. Geochim. Cosmochim. Acta 60, 1709–1725.

Bell, K., Lavecchia, G., Rosatelli, G., 2013. Cenozoic Italian magmatism – Isotope constraints for possible plume-related activity. J. S. Am. Earth Sci. 41, 22–40. https://doi.org/10.1016/j.jsames.2012.10.005.

Brozzetti, F., Cirillo, D., Liberi, F., Piluso, E., Faraca, E., De Nardis, R., Lavecchia, G., 2017. «Structural Style of Quaternary Extension in the Crati Valley (Calabrian Arc): Evidence in support of an East-Dipping Detachment Fault. Ital. J. Geosci., Vol. 136, No. 3 (2017), pp. 434-453, 12 figs. doi: 10.3301/IJG.2017.11.

Bello, S., Lavecchia, G., Andrenacci, C., Ercoli, M., Cirillo, D., Carboni, F., Barchi, M.R., Brozzetti, F., 2022. Complex trans-ridge normal faults controlling large earthquakes. Scientific Reports 12, 10676. https://doi.org/10.1038/s41598-022-14406-4.

Burke, W.H., Denison, R.E., Hetherington, E.A., Koepnick, R.B., Nelson, H.F., Otto, J.B., 1982. Variations of seawater $^{87}Sr/^{86}Sr$ throughout Phanerozoic time. Geology 10, 516–519.

Carignan, J., Hild, P., Mevelle, G., Morel, J., Yeghicheyan, D., 2001. Routine analyses of trace elements in geological samples using flow injection and low-pressure on-line liquid chromatography coupled to ICP-MS: a study of geochemical reference materials BR, DR-N, UB-N, AN-G and GH. Geostand. Geoanal. Res. 25, 187–198.

Cebrià, J.M., Lopez-Ruiz, J., Doblas, M., Martins, L.T., Munha, J., 2003. Geochemistry of the early Jurassic Messejana-Plasencia dyke (Portugal–Spain); implications on the origin of the Central Atlantic Magmatic Province. J. Petrol. 44, 547–568.

Centamore, E., Crescenti, U., Dramis, F., 2006a. Servizio Geologico d'Italia, 2005. Carta geologica d'Italia alla scala 1:50.000; Foglio 369 - Sulmona. ISPRA, Roma.

Centamore, E., Crescenti, U., Dramis, F., 2006b. Servizio Geologico d'Italia, 2005. Carta geologica d'Italia alla scala 1:50.000; Foglio 360 – Torre de' Passeri. ISPRA, Roma.

Chao-Feng, L., Guo, J.-H., Yang, Y.-H., Chua, Z.-Y., X.-c.,, 2014. Single-step separation scheme and high-precision isotopic ratios analysis of Sr–Nd–Hf in silicate materials. J. Anal. At. Spectrom 8, 1467–1476.

Chen, J.H., Pallister, J.S., 1981. Lead isotopic studies of the Samail ophiolite, Oman. J. Geophys. Res. 86, 2699–2708.

Ciavardelli, D., D'Anniballe, G., Nano, G., Martin, F., Federici, G., Sacchetta, P., Di Ilio, C., Urbani, A., 2007. An inductively coupled plasma mass spectrometry method for the quantification of yttrium-antibody-based drugs using stable isotope tracing. Rapid Commun. Mass Spectrom. 21, 2343–2350.

Ciavardelli, D., Sacchetta, P., Federici, G., Di Ilio, C., Urbani, A., 2010. Protein phosphorylation stoichiometry by simultaneous ICP-QMS determination of phosphorus and sulfur oxide ions: a multivariate optimization of plasma operating conditions. Talanta 80, 1513–1525.

Cirrincione, R., Fiannacca, P., Lustrino, M., Romano, V., Tranchina, A., 2014. Late Triassic tholeiitic magmatism in Western Sicily: A possible extension of the Central Atlantic Magmatic Province (CAMP) in the Central Mediterranean area? Lithos 188, 60–71.

Cirrincione, R., Fiannacca, P., Lustrino, M., Romano, V., Tranchina, A., Villa, I.M., 2015. Enriched asthenosphere melting beneath the nascent North African margin: trace element and Nd isotope evidence in middle–late Triassic alkali basalts from central Sicily (Italy). Int. J. Earth Sci. 105, 595–609.

Compagnoni, B., Damiani, A.V., 1971. Note illustrative alla Carta geologica d'Italia alla scala 1:100.000, Foglio 220 Verbicaro. Arti Grafiche E. Di Mauro. Cava dei Tirreni.

Conticelli, S., Avanzinelli, R., Ammannati, E., Casalini, M., 2015. The role of carbon from recycled sediments in the origin of ultrapotassic igneous rocks in the Central Mediterranean. Lithos 232, 174–196. https://doi.org/10.1016/j.lithos.2015.07.002.

Cornacchia, I., Agostini, S., Brandano, M., 2018. Miocene oceanographic evolution based on the Sr and Nd isotope record of the Central Mediterranean. Paleoceanogr. Paleoclimatol. 33, 31–47.

Cosentino, D., Cipollari, P., Marsili, P., Scrocca, D., 2010. Geology of the Central Apennines: a regional review. J. Virtual Explor. 36 (11), 1–37.

DePaolo, D.J., Wasserburg, G.J., 1976. Neodymium isotopic variations and the petrogenetic models. Geophys. Res. Lett. 3, 249–252.

Dera, G., Prunier, J., Smith, P.L., Haggart, J.W., Popov, E., Guzhov, A., Rogovf, M., Delsate, D., Thies, D., Cuny, G., Pucéat, E., Charbonnier, G., Bayon, G., 2015. Nd isotope constraints on ocean circulation, paleoclimate, and continental drainage during the Jurassic breakup of Pangea. Gondw. Res. 27, 1599–1615.

Erel, Y., Harlavan, Y., Blum, J.D., 1994. Lead isotope systematics of granitoid weathering. Geochim. Cosmochim. Acta 58, 5299–5306.

Faure, G. Mensing, T.M., 2005. Isotopes. Principles and Application. 3rd Edition, John Wiley and Sons, Hoboken, New Jersey, pp. 897.

Frank, M., 2002. Radiogenic isotopes: tracers of past ocean circulation and erosional input. Rev. Geophys. 40, 1–38.

Frank, M., O'Nions, R.K., 1998. Sources of Pb for Indian Ocean ferromanganese crusts: a record of Himalayan erosion? Earth Planet. Sci. Lett. 158, 121–130.

Galeotti, S., Moretti, M., Cappelli, C., Phillips, J., Lanci, L., Littler, K., Monechi, S., Petrizzo, M.R., S., Isabella Premoli S., Zachos, J.C., 2013. The Bottaccione section at Gubbio, Central Italy: a classic Palaeocene Tethyan setting revisited. In: Rocha, R., Pais, J., Kullberg, J., Finney, S. (eds) STRATI 2013. Springer Geology. Springer, Cham. 10.1007/978-3-319-04364-7_21.

Gambacorta, G., Jenkyns, H.C., Russo, F., Tsikos, H., Wilson, P.A., Faucher, G., Erba, E., 2015. Carbon- and oxygen-isotope records of mid-Cretaceous Tethyan pelagic sequences from the Umbria – Marche and Belluno Basins (Italy). Newsl. Stratigr. 48, 299–323. https://doi.org/10.1127/nos/2015/0066.

Henderson, G.M., Maier-Reimer, E., 2002. Advection and removal of Pb-210 and stable Pb isotopes in the oceans: a general circulation model study. Geochim. Cosmochim. Acta 66, 257–272.

Huck, S., Heimhofer, U., Immenhauser, A., Weissert, H., 2013. Carbon-isotope stratigraphy of Early Cretaceous Urgonian) shoal-water deposits: Diachronous changes in carbonate-platform production in the north-western Tethys. Sed. Geol. 290, 157–174. https://doi.org/10.1016/j.sedgeo.2013.03.016.

Jenkyns, H.C., Clayton, C.J., 1986. Black shales and carbon isotopes in pelagic sediments from the Tethyan Lower Jurassic. Sedimentology 33, 87–106. https://doi.org/10.1111/j.1365-3091.1986.tb00746.x.

Lacan, F., Tachikawa, K., Jeandel, C., 2012. Neodymium isotopic composition of the oceans: a compilation of seawater data. Chem. Geol. 300–301, 177–184.

Lavecchia, G., de Nardis, R., Ferrarini, F., Cirillo, D., Bello, S., Brozzetti, F., 2021. Regional seismotectonic zonation of hydrocarbon fields in active thrust belts: a case study from italy. Book Chapter NATO Sci. Peace Secur. Ser. C: Environ. Secur. 2021, 89–128.

Lavecchia G., Bello S., Andrenacci C., Cirillo D., Ferrarini F., Vicentini N., de Nardis R., Roberts G., Brozzetti F., (2022). "QUaternary fault strain INdicators database - QUIN 1.0 - first release from the Apennines of central Italy".

Lawrence, M.G., Greig, A., Collerson, K.D., Kamber, B.S., 2006. Rare earth element and yttrium variability in South East Queensland waterways. Aquat. Geochem. 12, 39–72.

Madhavaraju, J., González-León, C.M., 2012. Depositional conditions and source of rare earth elements in carbonate strata of the Aptian-Albian Mural Formation, Pitaycachi section, northeastern Sonora, Mexico. Revista Mexicana de Ciencias Geologicas 29, 478–491.

Madhavaraju, J., Loser, H., Lee, Y.I., Santacruz, R.L., Pi-Puig, T., 2016. Geochemistry of Lower Cretaceous limestones of the Alisitos Formation, Baja California, Mexico: implications for REE source and paleo-redox conditions. J. S. Am. Earth Sci. 66, 149–165.

Mahoney, J.J., Frei, R., Tejada, M.L.G., Mo, X.X., Leat, P.T., Näglerm, T.F., 1998. Tracing the Indian Ocean mantle domain through time: isotopic results from old West Indian, East Tethyan, and South Pacific seafloor. J. Petrol. 39, 1285–1306. https://doi.org/10.1093/petroj/39.7.1285.

McArthur, J.M., Howart, R., Bailey, T., 2001. Strontium Isotope Stratigraphy: LOWESS version 3: best fit to the marine Sr-isotope curve for 0–509 Ma and accompanying look-up table for deriving numerical age. J. Geol. 109, 155–170.

McLennan, S.M., 2001. Relationships between the trace element composition of sedimentary rocks and upper continental crust. Geochem. Geophys. Geosyst. 2, 1021.

Mirnejad, H., Bell, K., 2006. Origin and source evolution of the Leucite Hills lamproites: Evidence from Sr-Nd-Pb-O isotopic compositions. J. Petrol. 47, 2462–2489.

Moretti, M., Pieri, P., Ricchetti, G., Spalluto, L., 2011. Note illustrative della Carta Geologica d'Italia alla scala 1:50.000, foglio 396 San Severo, Servizio Geologico d'Italia. Litografia Artistica Cartografica srl.

Morsilli, M., 2016. Sintesi delle conoscenze geologiche e stratigrafiche del promontorio del Gargano. Geologi e territorio, Ordine Regionale dei Geologi – Puglia, n° 2, 15-30.

Muiños, S.B., Frank, M., Maden, C., Hein, J.R., van de Flierdt, T., Lebreiro, S.M., Gaspar, L., Monteiro, J.H., Halliday, A.N., 2008. New constraints on the Pb and Nd isotopic evolution of NE Atlantic water masses. Geochem. Geophys. Geosyst. 9, Q02007. https://doi.org/10.1029/2007GC001766.

Nagarajan, R., Madhavaraju, J., Armstron-Altrin, J.S., Nagendra, R., 2011. Geochemistry of Neoproterozoic limestones of the Shahabad Formation, Bhima Basin, Karnataka, southern India. Geosci. J. 15, 9–25.

Noble, A.E., Echegoyen-Sanz, Y., Boyle, E.A., Ohnemus, D.C., Lam, P.J., Kayser, R., Reuer, M., Wu, J., 2015. Dynamic variability of dissolved Pb and Pb isotope composition from the U.S. North Atlantic GEOTRACES Transect. Deep-Sea Research Pt. 116, 208–225. doi: 10.1016/j.dsr2.2014.11.011 2015.

Owen, J.P., 2006. Mineralogy, petrology, and isotope geochemistry of magmatic rocks from the Western Alps, Ernici and Roccamonfina, Italy: Constraints on mantle enrichment processes. Unpublished Ph.D. Thesis, Carleton University, Ottawa, 452 pp.

Patacca, E., Scandone, P., Di Luzio, E., Cavinato, G.P., Parotto, M., 2008. Structural architecture of the central Apennines: interpretation of the CROP 11 seismic profile from the Adriatic coast to the orographic divide. Tectonics 27 (3).

Pin, C., Zalduegui, J., 1997. Sequential separation of light-rare-earth elements, thorium and uranium by miniaturized extraction chromatography: application to isotopic analyses of silicate rocks. Anal. Chim. Acta 339, 79–89.

Piper, D.Z., Bau, M., 2013. Normalized Rare Earth Elements in water, sediments, and wine: identifying sources and environmental redox conditions. Am. J. Anal. Chem. 4, 69–83.

Pourmand, A., Dauphas, N., Ireland, T.J., 2012. A novel extraction chromatography and MC-ICP-MS technique for rapid analysis of REE, Sc and Y: revising CI-chondrite and Post-Archean Australian Shale (PAAS) abundances. Chem. Geol. 291, 38–54. https://doi.org/10.1016/j.chemgeo.2011.08.011.

Raulin, C., Frizon, de Lamotte, D., Bouaziz, S., Khomsi, S., Mouchot, N., Ruiz, G., Guillocheau, F., 2011. Late Triassic–early Jurassic block tilting along E–W faults, in southern Tunisia: New interpretation of the Tebaga of Medenine. J. African Earth Sci. 61. 94–104.

Rosatelli, G., Wall, F., Stoppa, F., 2007. Calcio-carbonatite melts and metasomatism in the mantle beneath Mt. Vulture (Southern Italy). Lithos 99, 229–248. https://doi.org/10.1016/j.lithos.2007.05.011.

Rottura, A., Bargossi, G.M., Caggianelli, A., Del Moro, A., Visonà, D., Tranne, C.A., 1998. Origin and significance of the Permian high-K calc-alkaline magmatism in the central-eastern Southern Alps, Italy. Lithos 45, 329–348.

Scandone, P., 1971. Note illustrative della Carta Geologica d'Italia alla scala 1:100.000: Fogli 199 e 210 "Potenza e Lauria". Servizio Geologico d'Italia, 71 p. Roma.

Schettino, A., Turco, E., 2011. Tectonic history of the western Tethys since the Late Triassic. GSA Bull. 123, 89–105. https://doi.org/10.1130/B30064.1.

Sharma, M., Wasserburg, G.J., 1996. The neodymium isotopic compositions and rare earth patterns in highly depleted ultramafic rocks. Geochim. Cosmochim. Acta 60, 4537–4550.

Silver, L.T., Woodhead, J.A., Williams, I.S., Chappell, B.W., 1984. Uranium in granites from the southwestern United States: Actinide parent-daughter systems, sites and mobilization, D AC13-76GIO1664D, ep. of Energy,W ashington D.C.

Shields, G., Stille, P., 2001. Diagenetic constraints on the use of cerium anomalies as palaeoseawater redox proxies: an isotopic and REE study of Cambrian phosphorites. Chem. Geol. 175, 29–48.

Spalluto, L., Pieri, P., Ricchetti, G., 2005. Le facies carbonatiche di piattaforma interna del Promontorio del Gargano: implicazioni paleoambientali e correlazioni con la coeva successione delle Murge (Italia meridionale, Puglia).". Bollettino-Società Geologica Italiana 124 (3), 675.

Stampfli, G.M., Borel, G.D., 2002. A plate tectonic model for the Paleozoic and Mesozoic constrained by dynamic plate boundaries and restored synthetic oceanic isochrons. Earth Planet. Sci. Lett. 196, 17–33.

Stoppa, F., Alexei, S., Rukhlov, A.S., Bell, K., Schiazza, M., Vichi, G., 2014. Lamprophyres of Italy: early Cretaceous alkaline lamprophyres of Southern Tuscany, Italy. Lithos 188, 97–112. https://doi.org/10.1016/j.lithos.2013.10.010.

Stoppa, F., Schiazza, M., Rosatelli, G., Castorina, F., Sharygin, V.V., Ambrosio, F.A., Vicentini, N., 2019. Italian carbonatite system: From mantle to ore-deposit. Ore Geol. Rev. 114, 103041 https://doi.org/10.1016/j.oregeorev.2019.103041.

Stumpf, R., Frank, M., Schonfeld, J., Haley, B.A., 2010. Late Quaternary variability of Mediterranean Outflow Water from radiogenic Nd and Pb isotopes. Quat. Sci. Rev. 29, 2462–2472.

Tavani, S., Iannace, A., Mazzoli, S., Vitale, S., Parente, M., 2013. Late Cretaceous extensional tectonics in Adria: insights from soft-sediment deformation in the Sorrento Peninsula (southern Apennines). J. Geodyn. 68, 49–59.

Taylor, S.R., McLennan, S.M., 1985. The Continental crust: its composition and evolution. Oxford, Blackwell, p. 349 pp..

Tostevinet, R., Shields, G.A., Tarbuck, G.M., He, T., Clarkson, M.O., Woods, R.A., 2016. Effective use of cerium anomalies as a redox proxy in carbonate-dominated marine settings. Chem. Geol. 438, 146–162.

van de Flierdt, T., Frank, M., Halliday, A.N., Hein, J.R., Hattendorf, B., Günther, D., Kubik, P.W., 2004. Tracing the history of submarine hydrothermal inputs and the significance of hydrothermal afnium for the seawater budget—a combined Pb–Hf–Nd isotope approach. Earth Planet. Sci. Lett. 222, 259–273.

Veizer, J., 1983. Chemical diagenesis of carbonates: theory and application of trace element technique. Stable Isotopes. Sed. Geol. SC10, 3.1-3.100.

Veizer, J., Ala, D., Azmy, K., Bruckschen, P., Buhl, D., Bruhn, F., Carden, G.A.F., Diener, A., Godderis, S.E.Y., Jasper, T., Korte, C., Pawellek, F., Podlaha, O.G., Strauss, H., 1999. $^{87}Sr/^{86}Sr$, $\delta^{13}C$ and $\delta^{18}O$ evolution of Phanerozoic seawater. Chem. Geol. 161, 59–88.

Veizer, J., Godderis, Y., Francois, L.M., 2000. Evidence for decoupling of atmospheric CO_2 and global climate during the Phanerozoic eon. Nature 408, 698–701.

Vitale, S., Amore, O.F., Ciarcia, S., Fedele, L., Grifa, C., Prinzi, E.P., Tavani, S., D'Assisi, T., 2017. Structural, stratigraphic, and petrological clues for a Cretaceous-Paleogene abortive rift in the southern Adria domain (southern Apennines, Italy). Geological Journal. XXX 1–22. https://doi.org/10.1002/gj.2919.

Vitale, S., Prinzi, E.P., D'Assisi Tramparulo, F., De Paola, C., Di Maio, R., Piegari, E., Sabbatino, M., Natale, J., Notaro, P., Ciarcia, S., 2020. Late Miocene-Early Pliocene out of sequence thrusting in the Southern Apennines (Italy). Geosciences 10, 301. https://doi.org/10.3390/geosciences10080301.

von Blanckenburg, F., Nägler, T.F., 2001. Weathering versus circulation-controlled changes in radiogenic isotope tracer composition of the Labrador Sea and Atlantic Deep Water. Paleoceanography 16, 424–434.

Wilson, M., Shimron, A.E., Rosenbaum, J.M., Preston, J., 2000. Early Cretaceous magmatism of Mount Hermon, Northern Israel. Contrib. Miner. Petrol. 139, 54–67.

Xu, J.-F., Castillo, P.R., 2004. Geochemical and Nd–Pb isotopic characteristics of the Tethyan asthenosphere: implications for the origin of the Indian Ocean mantle domain. Tectonophysics 393, 9–27.

Zarcone, G., Petti, F.M., Cillari, A., Di Stefano, P., Guzzetta, D., Nicosia, U., 2010. A possible bridge between Adria and Africa: New palaeobiogeographic and stratigraphic constraints on the Mesozoic paleogeography of the Central Mediterranean area. Earth Sci. Rev. 103 (3–4), 154–162.

Zhang, K.-J., Li, Q.-H., Yan, L.-L., Zeng, L., Lu, L., Zhang, Y.-X., Hui, J., Jin, X., Tang, X.-C., 2017. Geochemistry of limestones deposited in various plate tectonic settings. Earth Sci. Rev. 167, 27–46.

Zhang, S.-Q., Mahoney, J.J., Mo, X.-X., Ghazi, A.M., Milani, L., Crawford, A.J., Guo, T.-Y., Zao, Z.-D., 2005. Evidence for a widespread Tethyan upper mantle with Indian-Ocean-Type isotopic characteristics. J. Petrol. 46, 829–858.